

The recent decline and recovery of Indian summer monsoon rainfall: relative roles of external forcing and internal variability

Article

Accepted Version

Huang, X., Zhou, T., Turner, A. ORCID: <https://orcid.org/0000-0002-0642-6876>, Dai, A., Chen, X., Clark, R., Jiang, J., Man, W., Murphy, J., Rostron, J., Wu, B., Zhang, L., Zhang, W. and Zou, L. (2020) The recent decline and recovery of Indian summer monsoon rainfall: relative roles of external forcing and internal variability. *Journal of Climate*, 33 (12). pp. 5035-5060. ISSN 1520-0442 doi: <https://doi.org/10.1175/JCLI-D-19-0833.1> Available at <https://centaur.reading.ac.uk/89465/>

It is advisable to refer to the publisher's version if you intend to cite from the work. See [Guidance on citing](#).

To link to this article DOI: <http://dx.doi.org/10.1175/JCLI-D-19-0833.1>

Publisher: American Meteorological Society

All outputs in CentAUR are protected by Intellectual Property Rights law, including copyright law. Copyright and IPR is retained by the creators or other copyright holders. Terms and conditions for use of this material are defined in the [End User Agreement](#).

www.reading.ac.uk/centaur

CentAUR

Central Archive at the University of Reading

Reading's research outputs online

The Recent Decline and Recovery of Indian Summer Monsoon Rainfall:

Relative Roles of External Forcing and Internal Variability

Xin HUANG^{1,2}, Tianjun ZHOU^{1,2,3*}, Andrew TURNER⁴, Aiguo DAI⁵,

Xiaolong CHEN¹, Robin CLARK⁶, Jie JIANG^{1,2}, Wenmin MAN^{1,3}, James MURPHY⁶,

John ROSTRON⁶, Bo WU^{1,3}, Lixia ZHANG^{1,3}, Wenxia ZHANG¹, Liwei ZOU^{1,3}

1 LASG, Institute of Atmospheric Physics, Chinese Academy of Sciences, Beijing 10029, China

2 University of Chinese Academy of Sciences, Beijing 100049, China

*3 CAS Center for Excellence in Tibetan Plateau Earth Sciences, Chinese Academy of Sciences
(CAS), Beijing 100101, China*

*4 National Centre for Atmospheric Science and Department of Meteorology, University of Reading,
Reading RG6 6BB, United Kingdom*

*5 Department of Atmospheric and Environmental Sciences, University at Albany, State University of
New York, Albany, NY, USA*

6 Met Office Hadley Centre, Exeter, EX1 3PB, United Kingdom

Corresponding author:

Dr. Tianjun ZHOU

LASG, Institute of Atmospheric Physics

Chinese Academy of Sciences

Beijing 100029, China.

Phone: 86-10-8299-5279

Fax: 86-10-8299-5172

E-mail: zhoutj@lasg.iap.ac.cn

ORCID ID: <https://orcid.org/0000-0002-5829-7279>

29

Abstract

30 The Indian summer monsoon (ISM) rainfall affects a large population in South Asia. Observations
31 show a decline in ISM rainfall from 1950-1999 and a recovery from 1999-2013. While the decline has
32 been attributed to global warming, aerosol effects, deforestation, and a negative-to-positive phase
33 transition of the Interdecadal Pacific Oscillation (IPO), the cause for the recovery remains largely
34 unclear. Through analyses of a 57-member perturbed-parameter ensemble of model simulations, this
35 study shows that the externally-forced rainfall trend is relatively weak and is overwhelmed by large
36 internal variability during both 1950-1999 and 1999-2013. The IPO is identified as the internal mode
37 that helps modulate the recent decline and recovery of the ISM rainfall. The IPO induces ISM rainfall
38 changes through moisture convergence anomalies associated with an anomalous Walker circulation
39 and meridional tropospheric temperature gradients and the resultant anomalous convection and zonal
40 moisture advection. The negative-to-positive IPO phase transition from 1950-1999 reduces what
41 would have been an externally-forced weak upward rainfall trend of $0.01 \text{ mm day}^{-1} \text{ decade}^{-1}$ to -0.15
42 $\text{mm day}^{-1} \text{ decade}^{-1}$ during that period, while the rainfall trend from 1999-2013 increases from the
43 forced value of 0.42 to $0.68 \text{ mm day}^{-1} \text{ decade}^{-1}$ associated with a positive-to-negative IPO phase
44 transition. Such a significant modulation of the historical ISM rainfall trends by the IPO is confirmed
45 by another 100-member ensemble of simulations using perturbed initial conditions. Our findings
46 highlight that the interplay between the effects of external forcing and the IPO needs be considered for
47 climate adaptation and mitigation strategies in South Asia.

48

49 **1. Introduction**

50 More than a fifth of the world's population lives on the Indian subcontinent and depends on the
51 Indian summer monsoon (ISM) for their water supply (Singh et al. 2019). The ISM provides about 80%
52 of the annual rainfall to South Asia and is the strongest component of the global monsoon system
53 (Wang et al. 2017). Thus, understanding of ISM variability on different time scales is critical for
54 effective risk management and adaptation planning in this densely populated and ecologically
55 vulnerable region (Turner and Annamalai 2012).

56 The greatest ISM rainfall occurs over the Western Ghats, over the Himalayan foothills, in the core
57 monsoon region over north-central India (NCI) and along the Burmese coast (Fig. 1a, c, e). Variations
58 of summer rainfall over the core monsoon zone are widely used to measure the variability of the ISM
59 (Gadgil 2003; Goswami et al. 2006; Bollasina et al. 2011; Jiang and Ting 2017). During the second
60 half of the 20th century, summer rainfall decreased significantly over the NCI region, accompanied by
61 a weakening of the large-scale ISM circulation (Bollasina et al. 2011; Salzmman et al. 2014; Roxy et
62 al. 2015; Salzmman and Cherian 2015). Since the early 2000s however, the drying trend in NCI has
63 ceased together with a revival of the ISM circulation (Jin and Wang 2017; Roxy 2017).

64 The observed long-term decline of rainfall over India in the latter half of the 20th century has
65 been studied extensively. Several studies have attributed this to rapidly increasing anthropogenic
66 aerosol loading, which slows down the monsoon meridional overturning circulation by reducing the
67 land-ocean thermal contrast and inter-hemispheric energy imbalance (Bollasina et al. 2011; Salzmman
68 et al. 2014; Guo et al. 2015; Li et al. 2015). Global warming from greenhouse gas (GHG) forcing
69 increases atmospheric moisture holding capacity by virtue of the Clausius-Clapeyron relation.
70 Combined with small changes in atmospheric relative humidity (Collins et al. 2013), this leads to

71 increased water vapour and thus increased moisture convergence and rainfall during the ISM (May
72 2010; Li et al. 2015). Different sea surface temperature (SST) warming patterns can also displace
73 regions of convection and moisture transport, contributing to the regional precipitation response (Xie
74 et al. 2010). For example, warming over the tropical Indo-Pacific warm pool displaces South Asian
75 rainfall with an east-west rainfall shift by inducing anomalous northerlies, which advect drier and
76 cooler air into South Asia (Annamalai et al. 2013). Changes in land use and land cover have also been
77 proposed as another contributor: Local evapotranspiration, a source of atmospheric moisture, has
78 decreased as a consequence of deforestation (Paul et al. 2016; Chou et al. 2018). In addition to the
79 above anthropogenic forcings, a negative-to-positive phase transition from the 1950s to the 1990s of
80 the Pacific Decadal Oscillation (PDO)/Interdecadal Pacific Oscillation (IPO), whose recent cycles
81 result mainly from internal variability (Dong et al. 2014; Hua et al. 2018), also helps to explain the
82 total drying trend over India during this period, as highlighted by Salzmänn and Cherian (2015). Using
83 the multi-model ensemble from the 5th Coupled Model Intercomparison Project (CMIP5), the NCI
84 drying trend associated with the PDO/IPO was comparable to that caused by anthropogenic aerosols
85 derived from the single-forcing experiments during the period 1950-1999 (Salzmänn et al. 2014).

86 Compared with the extensive research focusing on the drying during 1950-1999, few studies have
87 examined the subsequent recovery of the ISM rainfall after 2000; Jin and Wang (2017) is an exception.
88 They found that ISM rainfall shows a positive trend after around 2000 with positive anomalies lasting
89 for multiple years, a situation that has never been observed since 1950 (Jin and Wang 2017). Thus, the
90 recent revival of the ISM in observations differs in character from the previous decadal variations. The
91 accelerated warming seen over South Asia that exceeds the tropical Indian Ocean warming is
92 considered as the main driver of the ISM revival (Jin and Wang 2017; Roxy 2017). Potential causes

93 for the recent warming over India include a reduction of low clouds due to decreased ocean evaporation
94 in the Arabian Sea (Jin and Wang 2017), an increase of anthropogenic aerosols, particularly those from
95 absorbing aerosols such as black carbon (Jin et al. 2016), changes in land-use and land cover (Paul et
96 al. 2016), and the strengthening GHG warming effect and its dominance over other drivers (Kitoh et
97 al. 2013). Although the observed revival of ISM rainfall appears to be underpinned by several factors,
98 few CMIP5 models are able to reproduce the recent trend (Jin and Wang 2017). It is not entirely
99 surprising considering the model performance in capturing the drying trend during 1950-1999 as
100 suggested by Guo et al. (2015), Saha et al. (2014) and Salzmman and Cherian (2015). One of the
101 explanations to the poor performance is that the externally-forced wetting trend after 2000 may be
102 overshadowed by internal variability in individual model realizations. Since CMIP5 model historical
103 simulations were not initialized from observed values, their output is not expected to match with
104 observations, particularly of changes in phase associated with interannual and decadal variability.
105 While the exact cause for the decline in ISM rainfall during 1950-1999 is still under debate, the relative
106 contributions of external forcing and internal variability to its revival after 2000 remain unknown.

107 At a larger scale, the overall Northern Hemisphere summer monsoon rainfall, which also
108 witnessed a recovery since the 1980s, has been partially attributed to internal variability in the Pacific
109 (Wang et al. 2013). The PDO/IPO is the main internal mode in the Pacific on interdecadal time scales,
110 which has been linked to decadal-to-multidecadal oscillations of the ISM (Krishnan and Sugi 2003;
111 Krishnamurthy and Krishnamurthy 2013; Joshi and Pandey 2011; Joshi and Rai 2015; Joshi and
112 Kucharski 2017). From the 1950s to the present, the PDO/IPO has experienced a negative-to-positive-
113 to-negative phase transition (Mantua and Hare 2002; Dong and Dai 2015; Henley et al. 2015; Joshi
114 and Rai 2015). The positive PDO/IPO phase appears to be related to decreased ISM rainfall through

115 weakened Walker and Hadley circulations induced by warm SST anomalies over the tropical central-
116 eastern Pacific, and the opposite occurs for the IPO negative phase (Krishnan and Sugi 2003;
117 Krishnamurthy and Krishnamurthy 2013; Dong and Dai 2015; Joshi and Kucharski 2017). The
118 PDO/IPO can also influence the interannual variability of ISM rainfall by enhancing the El Niño-
119 Southern Oscillation (ENSO)-ISM relationship when ENSO and PDO/IPO are in phase, while
120 weakening the relationship when out of phase (Krishnan and Sugi 2003; Krishnamurthy and
121 Krishnamurthy 2013; Dong et al. 2018). It is unclear whether the PDO/IPO is the dominant internal
122 mode responsible for both the interdecadal decline and recovery of ISM rainfall since 1950.

123 Determining the role of internal variability requires the exclusion of the externally-forced
124 signal. Previous studies rely heavily on the multi-model ensemble of CMIP5 with small numbers (<10)
125 of realizations from individual models (Salzmann and Cherian 2015; Jin and Wang 2017). Different
126 CMIP models may include different implementations of the forcings and also differ in their dynamical
127 cores and physical parameterizations, which complicate the interpretation of the differences among
128 individual simulations (Frankcombe et al. 2015; Dai and Bloecker 2019). Large differences exist in
129 simulating the recent decline and recovery of ISM rainfall not only among different CMIP5 models
130 but also among different realizations from individual models (Saha et al. 2014; Salzmann and Cherian
131 2015; Jin and Wang 2017). This hampers understanding of the relative role of internal variability and
132 external forcing. To avoid these issues, a large ensemble from a single climate model is a more suitable
133 tool for quantifying the internal variability and identifying the role of internal modes (Deser et al. 2012;
134 Dai and Bloecker 2019). Here, we use a 57-member perturbed-parameter ensemble of simulations
135 from the Earth system model HadCM3C (ESPPE) (Murphy et al. 2014). The relatively large ensemble
136 size allows us to consider its ensemble mean as the externally-forced signal, whilst the deviation of an

137 individual member from the ensemble mean results primarily from internal variability and secondly
138 from its own uncertain forced response (due to parameter uncertainty) (Murphy et al. 2004). To avoid
139 model dependence, we also analyzed the output from a 100-member ensemble of simulations
140 generated by the Max Planck Institute Earth System Model version 1.1 (MPI-ESM) with slightly
141 different initial conditions (Maher et al. 2018; Maher et al. 2019). In this study, we therefore aim to
142 answer the following questions: (1) what are the relative contributions of external forcing and internal
143 variability to the recent interdecadal variations in ISM rainfall? And (2) what are the differences and
144 similarities of the physical mechanisms responsible for the decline in ISM rainfall during 1950-1999
145 and its recovery during 1999-2013?

146 The remainder of the paper is organized as follows. In section 2, we describe the observational data,
147 model data and analysis methods. In section 3, we investigate the influence of external forcing on the
148 recent interdecadal variations of the ISM rainfall and its related physical processes. The influence of
149 internal variability, the dominant contribution from the IPO and the underlying mechanisms are
150 examined in section 4. In section 5, we quantify the contributions of external forcing and the observed
151 IPO transitions to the interdecadal variations of ISM rainfall. Results derived from different large
152 ensembles of model simulations are compared for robustness in section 6. A summary is given in
153 section 7.

154 **2. Data, methods, and models**

155 *a. Observational data*

156 The following observational monthly gridded rainfall data are used in this study:

157 1) CRU version 4.02 from the Climatic Research Unit at the University of East Anglia, covering the

158 period of 1901-2017 with a horizontal resolution of $0.5^{\circ} \times 0.5^{\circ}$ (Harris et al. 2014).

159 2) GPCC monthly product version 2018 from the Global Rainfall Climatology Centre dataset,
160 covering the period of 1891-2016 with a horizontal resolution of $0.5^{\circ} \times 0.5^{\circ}$ (Schneider et al. 2014).

161 3) UDel version 5.01 from University of Delaware, covering the period of 1900-2017 with a
162 horizontal resolution of $0.5^{\circ} \times 0.5^{\circ}$ (Willmott and Matsuura 2001).

163 Here, we calculated the average of the three datasets over the period of 1901-2017 (except for
164 2017, since at the time of writing GPCC ends in 2016) as the observational rainfall data (referred to as
165 OBS) following previous studies (Huang et al. 2019; Jiang and Zhou 2019). The average OBS is
166 interpolated to the model's resolution to compare with the model results. Results for each dataset at
167 the raw resolutions are also shown in Fig. 1 and Fig. 3.

168 Observed monthly sea surface temperature (SST) data were taken from the Hadley Centre Global
169 Sea Ice and Sea Surface Temperature (HadISST1.1) dataset produced by the Met Office, starting from
170 1870 up to the present with a horizontal resolution of $1.0^{\circ} \times 1.0^{\circ}$ (Rayner et al. 2003). Monthly global
171 land-surface air temperature anomalies with respect to the 1961-90 average were taken from
172 CRUTEM4 produced by the Climatic Research Unit at the University of East Anglia, starting from
173 1850 to present at a resolution of $5.0^{\circ} \times 5.0^{\circ}$ (Jones et al. 2012).

174 Monthly atmospheric reanalysis data were obtained from the National Centers for Environmental
175 Prediction (NCEP)–National Center for Atmospheric Research (NCAR) reanalysis dataset
176 (NCEP/NCAR) (Kalnay et al. 1996).

177 To capture the interdecadal variability in the Pacific, we used two published indices in this study
178 for comparison. One is the PDO index from Mantua and Hare (2002; accessed at

179 <http://www.jisao.washington.edu/pdo>), and the other is the Tripole Index (TPI) from Henley et al (2015;
180 accessed at <https://www.esrl.noaa.gov/psd/data/timeseries/IPOTPI>).

181 ***b. Model Data***

182 ***(1) ESPPE***

183 We used output from a 57-member Earth system perturbed parameter ensemble (ESPPE) (Murphy
184 et al. 2014). The ESPPE simultaneously and selectively perturbs multiple parameters within expert-
185 specified limits in the atmosphere, ocean, sulphur cycle and terrestrial ecosystem components of the
186 Earth system model HadCM3C, which contains a fully interactive carbon cycle and an interactive
187 sulphur cycle scheme. The model includes the direct scattering and absorption effects along with the
188 cloud albedo effect of aerosols (first indirect effect), while the aerosol-rainfall efficiency effect (second
189 indirect effect) is excluded. The 57 members of the ESPPE are model variants of HadCM3C, with
190 regular latitude-longitude grids of $2.5^{\circ} \times 3.75^{\circ}$ and $1.25^{\circ} \times 1.25^{\circ}$ in the atmosphere and ocean, with 19
191 and 20 vertical levels respectively (Gordon et al. 2000). Each member is spun up from an identical
192 initial state taken from a standard HadCM3C run, providing starting conditions for the ESPPE
193 simulations of forced climate change (Lambert et al. 2013). The historical simulations of ESPPE are
194 integrated from 1860 to 2005 driven by observed historical changes in radiative forcing agents such as
195 emissions of CO₂ and aerosol precursors, ozone, solar variations and major volcanic eruptions
196 following CMIP5 protocol (Taylor et al. 2012). The RCP8.5 simulations, where the radiative forcing
197 increases and reaches around 8.5 W/m² near 2100 relative to 1750, are then performed from 2006 to
198 2099 continuously following each of the 57 members of the historical run. Details of the spin-up and
199 the perturbed parameters are provided in Lambert et al. (2013).

200 Compared to its contemporaries, ESPPE's parent model, HadCM3, is one of the best at simulating
201 the spatial pattern of ISM rainfall (Annamalai et al. 2007), the spatial structure of the IPO and the IPO-
202 ISM rainfall teleconnections (Joshi and Kucharski 2017). The ESPPE also reasonably simulates the
203 climatology of ISM rainfall (Fig. 1g). The climatological monsoon rainfall centers-of-action located
204 near the Western Ghats, over the foothills of the Himalayas and along the Burmese coast are well
205 simulated, aiding confidence in our further analysis based on this model. More detailed information
206 and a full evaluation of model performance for ESPPE is described in Murphy et al. (2014).

207 **(2) MPI-ESM**

208 To verify the results derived from the ESPPE, we also analyzed the output from a 100-member
209 ensemble generated by the Max Planck Institute Earth System Model version 1.1 (MPI-ESM) with
210 slightly different initial conditions (Maher et al. 2018; Maher et al. 2019). It is an update of the coupled
211 ocean-atmosphere general circulation model submitted to CMIP5 in its low resolution configuration
212 (MPI-ESM-LR), which has a spectral horizontal resolution of T63 ($\sim 1.9^\circ$) and 47 vertical layers up to
213 0.01hPa in the atmosphere along with 1.5° horizontal resolution and 40 vertical levels in the ocean.
214 The 100 ensemble members started from different initial conditions in 1850, generated from different
215 years of the preindustrial control simulation (piControl). The historical simulations are then integrated
216 from 1850 to 2005 driven by observed historical changes in radiative forcing agents, including well-
217 mixed greenhouse gases, anthropogenic sulphate aerosols, man-made land use change, monthly zonal-
218 mean ozone concentrations and major volcanic eruptions following CMIP5 protocol (Taylor et al.
219 2012). The simulation was extended to 2099 following the RCP8.5 high emissions scenario. The MPI-
220 ESM reasonably reproduces the climatology of ISM rainfall (Fig. 1i), in addition to the IPO-related
221 SST patterns and the IPO-ISM rainfall relationship (Joshi and Kucharski 2017), providing further

222 confidence to the model.

223 *c. Methods*

224 *(1) Statistical analysis*

225 A 9-year-running mean was applied to observational and model data to isolate the interdecadal
226 signal. The Mann-Kendall (Mann 1945; Kendall 1975) non-parametric method was applied in this
227 study to test the significance of trends. The Monte Carlo non-parametric method was used to test the
228 significance of regression coefficients onto the filtered time series. A composite analysis was used to
229 calculate the average of the 10 members with the strongest positive (Pos10)/negative (Neg10) IPO
230 phase transitions. To test the significance of the trend differences between the Pos10 members and the
231 ensemble mean (and between Neg10 and the ensemble mean), the Student's t-test was used. Gridpoints
232 with at least 46 out of 57 ESPPE members or 80 out of 100 MPI-ESM members (80%) agreeing on
233 the sign of change are marked to indicate the consistency among ensemble members.

234 *(2) Separating the externally forced signal and internal variability using the large ensemble*

235 Let $A(i)$ be a given variable of member i from the ESPPE or MPI-ESM ensemble. Generally,
236 time series of $A(i)$ at each grid point can be viewed as consisting of an externally-forced component
237 (due to GHGs, aerosols, land use, solar cycles, and other external forcing) and an internally-unforced
238 component (due to internal climate variability). In both ESPPE and MPI-ESM, the ensemble members
239 were driven by the same external forcing. The ensemble means (EM) of $A(i)$ in each model can be
240 taken as the model's response to external forcing, because the averaging over the ensemble members
241 largely smooths out uncertainties among them. The model's forced response is represented as

242
$$A_{forced} = (A(i))_{EM} \quad (1).$$

243 The spread among the 100 MPI-ESM members is caused only by different realizations of the
244 internal variability. Thus, $A(i)$ of member i in MPI-ESM is separated as:

$$245 \quad A(i) = A_{forced} + A_{internal}(i), \quad i = 1,2,3 \dots 100 \quad (2)$$

246 where $A_{internal}(i)$ is the internal component estimated as the residual of the original $A(i)$ minus the
247 forced response. $A_{internal}(i)$ varies among different ensemble members and shows the variability
248 associated with internal variability.

249 The spread of climate changes obtained from various ESPPE members contains both uncertainty
250 in their forced response and internal variability arising from random climate variations (Murphy et al.
251 2004). Thus, $A(i)$ of member i in ESPPE is separated as:

$$252 \quad A(i) = A_{forced}(i) + A_{internal}(i), \quad i = 1,2,3 \dots 57 \quad (3)$$

253 where $A_{forced}(i)$ represents the response to external forcing within an individual member.
254 $A_{forced}(i)$ is different from the A_{forced} (the EM of the 57 members) in ESPPE due to uncertain
255 climate feedbacks caused by perturbed parameters. Several statistical methods have been suggested
256 for estimating the $A_{forced}(i)$, e.g., the linear trend, high-order polynomials approximation (Hawkins
257 and Sutton 2009, 2010) or using time series at each grid point linearly related to global-mean time
258 series of A (Dai et al. 2015). In this study, we calculated $A_{forced}(i)$ as a fourth-order polynomial of
259 time over the years 1860-2099 following Hawkins and Sutton (2009, 2010). We note that the estimated
260 $A_{forced}(i)$ may still contain some internal variability. However, since the polynomials were generated
261 over a long time period of 240 years, we consider $A_{forced}(i)$ as primarily consisting of the externally-
262 forced response.

263 **(3) IPO definition**

264 Previous studies show many different ways to calculate the index representing the PDO/IPO, for
265 example the EOF method (Mantua and Hare 2002) and the difference of SST anomalies between
266 regions of the Pacific (Henley et al. 2015; Salzmann and Cherian 2015), showing an overall similarity
267 in featuring the decadal-to-multidecadal variability of Pacific SST in observations after 1920 (Hua et
268 al. 2018). Thus, for easier calculation and for direct comparison between observations and model
269 simulations and comparison between ensemble members, we use the latter method to define the IPO
270 index without applying EOF analysis, similar to Salzmann and Cherian (2015). We define the IPO
271 index as the JJA south minus north gradient of unforced SST. In the observations, we first remove the
272 linear trend and then calculate the SST anomalies averaged within the tropical central-eastern Pacific
273 (TCEP, 170°W–90°W, 10°S–10°N) and the northern Pacific (NP, 150°E–150°W, 25°N–45°N),
274 respectively. The observational IPO index (IPO_{OBS}) is defined as the 9-year running mean of the
275 difference of detrended SST between the TCEP and the NP. Here, we used the terminology of *IPO* as
276 we focus on wider Pacific-basin phenomena. We assess the IPO index derived from the HadISST1.1
277 dataset and find that it is highly consistent with published PDO and TPI indices in terms of both phase
278 evolution and spatial pattern during our research period (Fig. 2).

279 In the ESPPE, we first separate out the internal part of SST, $SST_{internal}(i)$, based on equation
280 (3). The IPO index for member (i) is calculated as the 9-year running mean area-averaged difference
281 of JJA $SST_{internal}(i)$ between TCEP and NP. The IPO indices in the 57 ensemble members are
282 continuous time series with various IPO phase evolutions in the period 1950-2013. Here, we calculate
283 the trends of IPO indices in 1950-1999 and 1999-2013 respectively. During each period, positive
284 values represent the IPO shifting from negative to positive phases, while negative values show the
285 opposite. To identify the internal IPO mode in ESPPE, we choose the 10 members with the strongest

286 positive (Pos10) and strongest negative (Neg10) IPO phase transitions for composition during 1950-
 287 1999 and 1999-2013, respectively (Fig. 2f).

288 **(4) Adjustment of ISM rainfall trends based on IPO**

289 On the multi-decadal time scale, the contribution of the IPO to ISM rainfall trends of member i
 290 in the selected time period τ , for example $\tau = 1950\sim 1999, 1999\sim 2013$, is calculated as

291
$$\partial_t pr_{IPO}(i) = r_{pr,IPO}(i) \cdot \partial_t IPO(i), \quad i = 1,2,3 \dots 57 \text{ or } 100 \quad (4)$$

292
$$r_{pr,IPO}(i) = \frac{\partial pr(i)}{\partial IPO(i)}, \quad (5)$$

293 where $r_{pr,IPO}(i)$ is the regression coefficient of the 9-year running-mean rainfall with respect to the
 294 IPO time series of member i during the period of 1950-2013. Both ESPPE and MPI-ESM reasonably
 295 reproduce the negative correlation between the IPO and ISM rainfall found in observations and both
 296 have high consistency among ensemble members (Fig. 1). $\partial_t IPO(i)$ is the trend of the IPO(i) index
 297 over time period τ , representing the phase transition of IPO during the analysis period. $\partial_t pr_{IPO}(i)$ is
 298 the IPO-related rainfall trend of member i in period τ and varies among the ensemble members.

299 In order to achieve the rainfall trends influenced by both the external forcing and the observed
 300 IPO phase transition, we employ an adjustment method following Salzmann and Cherian (2015). We
 301 adjust the original rainfall trend based on Equation (4). After the adjustment, all ESPPE members are
 302 viewed as being influenced by the same observational IPO phase evolution during 1950-2013 instead
 303 of the random IPO transitions for the raw members. The adjusted rainfall trend of member i is the sum
 304 of the forced rainfall trend plus the internal component of the rainfall trend with an adjustment term
 305 depending on the difference between the simulated and observed IPO trends ($\partial_t IPO_{OBS}$), which is
 306 expressed as:

307
$$\partial_t pr_{adj}(i) = \partial_t pr_{forced} + \partial_t pr_{internal_adj}(i), \quad i = 1,2,3 \dots 57 \text{ or } 100 \quad (6)$$

308 where

309
$$\partial_t pr_{internal_adj}(i) = \partial_t pr_{internal}(i) + \alpha_{internal}(i), \quad (7)$$

310 where

311
$$\alpha_{internal}(i) = -r_{pr,IPO}(i) \cdot (\partial_t IPO(i) - \partial_t IPO_{OBS}), \quad (8)$$

312 where $\partial_t pr_{internal_adj}(i)$ is the adjusted internal rainfall trend calculated by adding the original
 313 internal trend to an adjustment term, $\alpha_{internal}(i)$. As shown in equation (8), the adjustment term takes
 314 the observational IPO phase transition into consideration. $\partial_t pr_{internal_adj}(i)$ can be viewed as the
 315 internal rainfall trends after replacing the raw IPO phase transitions with the observational one. Thus,
 316 the EM of the $\partial_t pr_{internal_adj}(i)$ represents the observed IPO's contribution to the rainfall trend. The
 317 IPO-adjusted total rainfall trend, $\partial_t pr_{adj}(i)$, is the sum of the simulated externally forced signal
 318 ($\partial_t pr_{forced}$) and the adjusted internal trend. After the above adjustment, the rainfall trend uncertainty
 319 among the 57 ESPPE members (or 100 MPI-ESM members) related to their random IPO phase
 320 transition is narrowed but the other internal uncertainty remains. The EM of $\partial_t pr_{adj}(i)$ represents
 321 the rainfall changes in response to external forcing and the observed IPO phase transition.

322 **(5) Moisture budget analysis**

323 The moisture-budget analysis method has been used in many studies (Chou and Neelin 2004;
 324 Chou et al. 2009; Seager et al. 2010). Here we apply it to understand the physical mechanisms
 325 governing historical changes in ISM rainfall. Using pressure-level coordinates, the moisture budget
 326 equation is expressed as:

327
$$\partial_t q = -P + E - \langle \nabla \cdot (\mathbf{V}q) \rangle + res \quad (9)$$

328 where $\partial_t q$ is the time derivative of vertically integrated moisture in the atmosphere, which is small
 329 and can be neglected. P and E are rainfall and evaporation, \mathbf{V} and q are horizontal winds and
 330 specific humidity; res is the residual term including the moisture transport by surface processes due
 331 to topography and transient eddies (Li et al. 2013). For long-term trends, equation (9) is mainly
 332 balanced by $P - E$ and $-\langle \nabla \cdot (\mathbf{V}q) \rangle$. Triangle parentheses indicate a vertical integration from the
 333 surface to the tropopause. $-\langle \nabla \cdot (\mathbf{V}q) \rangle$ refers to the vertically integrated moisture flux
 334 convergence. We separate $\mathbf{V} = \bar{\mathbf{V}} + \mathbf{V}'$ and $q = \bar{q} + q'$, where the overbars and primes indicate
 335 long-term means and departures, respectively, as is the convention. Equation (9) can be transformed
 336 to:

$$337 \quad P' - E' = -\langle \nabla \cdot (\bar{\mathbf{V}}q') \rangle -\langle \nabla \cdot (\mathbf{V}'\bar{q}) \rangle -\langle \nabla \cdot (\mathbf{V}'q') \rangle + res \quad (10)$$

338 where the first, second and third terms on the right-hand side of equation (10) denote thermodynamic,
 339 dynamic and nonlinear components of moisture convergence terms, separated from the total vertically
 340 integrated moisture flux convergence. They are contributed by changes of moisture only, circulation
 341 only and both moisture and circulation, respectively.

342 Considering the continuity equation, the dynamic components of moisture convergence can be
 343 further decomposed into three terms as:

$$344 \quad -\langle \nabla \cdot (\mathbf{V}'\bar{q}) \rangle = -\langle u' \partial_x \bar{q} \rangle -\langle v' \partial_y \bar{q} \rangle -\langle \omega' \partial_p \bar{q} \rangle \quad (11)$$

345 where u' , v' and ω' are the zonal wind, meridional wind and vertical pressure-velocity anomalies,
 346 respectively. The three terms on the right-hand side of equation (11) denote zonal, meridional and
 347 vertical dynamic components of the moisture convergence term, respectively.

348 **3. Impact of external forcing**

349 **3.1 Influence of external forcing on ISM rainfall trends**

350 From 1950 to 1999, a decreasing rainfall trend was seen over north-central India (NCI) in the
351 observations (Fig. 3a, b, c, m; significant in all datasets, except GPCC), consistent with previous
352 studies (Bollasina et al. 2011; Salzmann et al. 2014; Salzmann and Cherian 2015). The multi-dataset
353 average (referred to as OBS) trend is $-0.11 \text{ mm day}^{-1} \text{ decade}^{-1}$ for this period (Fig. 3g). To determine
354 the role of external forcing in this drying trend, we examined the ESPPE's ensemble mean (EM). The
355 EM can be considered as the response to external forcing. In the EM, a dipole pattern between a drying
356 trend close to the Himalayan foothills and a wetting trend further south was seen (Fig. 3h). The bipolar
357 rainfall change gave an overall insignificant trend of $0.01 \text{ mm day}^{-1} \text{ decade}^{-1}$ (p value is 0.55) over the
358 NCI, indicating little role of external forcing in the observed drying (Fig. 3n).

359 Following the decreasing trend, the observed NCI rainfall reversed to a significant increasing
360 trend during 1999-2013 (Fig. 3d, e, f), with a multi-dataset average of $0.66 \text{ mm day}^{-1} \text{ decade}^{-1}$ (Fig. 3j,
361 m). Unlike the drying trend, this recovery of monsoon rainfall was partially reproduced by the
362 ensemble mean of ESPPE. The EM shows a homogenous increasing trend over the NCI region of 0.42
363 $\text{mm day}^{-1} \text{ decade}^{-1}$ (Fig. 3k, 3n), indicating a role for external forcing in the observed revival during
364 this period.

365 **3.2 Physical mechanisms**

366 To explore why external forcing induces different rainfall trends during 1950-1999 and 1999-
367 2013, we compared the moisture budget terms of the two periods (Equations (9-10)). Figure 4a shows
368 quantitative results of the moisture budget analysis on the NCI rainfall trends. Rainfall change is
369 balanced by the changes of evaporation, dynamic and thermodynamic components and a nonlinear

370 term. The dynamic component is further separated into vertical, zonal and meridional dynamic
371 components of moisture convergence. During 1950-1999, opposing trends of dynamic and
372 thermodynamic moisture convergence lead to the weak NCI rainfall trend (Fig. 4a). Their spatial
373 patterns show that the thermodynamic component increases the NCI rainfall homogenously (Fig. 4d),
374 while the dynamic component results in the bipolar rainfall trend (Fig. 4b). Further decomposition of
375 the dynamic component shows that the dominant contribution comes from the vertical dynamic
376 moisture convergence (Fig. 4a, f), while the role of horizontal dynamic components is small (Fig. 4a,
377 h). In contrast to the pre-1999 period, the accumulative influence of the dynamic and thermodynamic
378 components results in the increasing rainfall trend after 1999 (Fig. 4a, c, e). Furthermore, the vertical
379 and zonal dynamic components comparably contribute to the increasing rainfall over southern and
380 northern India, respectively (Fig. 4a, g, i). These calculations reveal that while the thermodynamic
381 component related to changes in specific humidity is consistently increasing during the two periods,
382 the dynamic component indicating monsoon circulation changes caused by external forcing are
383 different.

384 We further investigated the interdecadal variations of specific humidity and monsoon circulation
385 caused by external forcing. During 1950-1999, atmospheric moisture content increased with GHG-
386 induced global warming (Fig. 5a, e, g), which explains the positive trend of the thermodynamic
387 component in this period. Meanwhile, a positive Indian Ocean (IO) dipole warming pattern was seen
388 with increased external forcing (Fig. 5e). The relatively larger warming trend in the western IO SST
389 helps maintain the anomalous easterly winds along the equator (Dong and Zhou 2014; Roxy et al.
390 2015). The divergent circulation induces anomalous descent and decreased rainfall from the Maritime
391 Continent to tropical southern IO (Fig. 5c). The rainfall is then increased over the western and southern

392 Indian subcontinent and adjacent seas due to anomalous moisture convergence associated with changes
393 in local Hadley-type circulation (Fig. 5c, 5g). Furthermore, the increased anthropogenic aerosols
394 subdue the warming over the Indian subcontinent as indicated in previous studies (Bollasina et al. 2011;
395 Guo et al. 2015; Jin and Wang 2017). The regional surface cooling near the Himalayan foothills
396 decreases local rainfall via the vertical dynamic term (Figs. 4f, 5e). Thus, the forced zonally
397 nonuniform warming over the tropical IO and local surface cooling together explain the bipolar trend
398 pattern of dynamic moisture convergence (Fig. 4b). Compared to the pre-1999 period, atmospheric
399 moisture content increased faster after 1999 due to enhanced global warming (Fig. 5b), resulting in a
400 larger positive trend in the thermodynamic component (Fig. 4e). Moreover, the most noticeable
401 difference in monsoon circulation changes between pre- and post-1999 period is the anomalous south-
402 easterly winds over the Bay of Bengal (Fig. 5c, 5d). After 1999, the stronger land-sea thermal contrast
403 between the East Asia and the western north Pacific Ocean intensifies the low-level subtropical
404 anticyclone and decreases rainfall over the western Pacific (Liu et al. 2012; Fig. 5d, 5f), which then
405 incites a Rossby wave to its west (Annamalai et al. 2013). The resultant anomalous south-easterly
406 winds over the Bay of Bengal dynamically increase rainfall over India by through inducing anomalous
407 ascent and moisture advection (Figs. 4g, 4i, 5d, 5h).

408 The above results suggest that external forcing has partially played a role in modulating the
409 interdecadal variations of ISM rainfall during 1950-2013. However, the insignificant rainfall trend
410 caused by external forcing from 1950-1999 is different from that observed. Also, the forced positive
411 trend after 1999 is relatively weaker than the OBS. These indicate the non-negligible contributions of
412 internal variability during both periods that shall be examined next.

413 **4. Impact of internal variability**

414 ***4.1 Influence of internal variability on ISM rainfall trends***

415 The spread of rainfall trends is large among the 57 members during both periods, as demonstrated
416 by the large standard deviations of rainfall trends across the ensemble members (Fig. 3i, l). Histograms
417 demonstrating spread in quantitative rainfall trends among the 57 members are show in Figure 6a and
418 6b. During 1950-1999, 27 of the 57 simulations show negative trends for NCI rainfall (Fig. 6a). The
419 NCI rainfall trends from the ensemble members range from -0.25 to 0.54 mm day⁻¹ decade⁻¹ during
420 this period. On the other hand, the spread among ensemble members ranges from -0.82 to 2.00 mm
421 day⁻¹ decade⁻¹ during 1999-2013 (Fig. 6b). Despite being forced by increasing GHG, there are still 14
422 out of the 57 ESPPE realizations that show negative NCI rainfall trends during this period. The spread
423 of ensemble members includes the influence of both the response uncertainty (due to uncertainties in
424 model parameters; $pr_{uncertain}(i)$) and internal variability ($pr_{internal}(i)$; Equation (3)). These two
425 different sources of uncertainty are partitioned with a fourth-order polynomial following previous
426 studies (Hawkins and Sutton 2009, 2010). After dividing the NCI rainfall trends into the above two
427 parts, the trend uncertainty caused by internal variability is larger than that caused by the uncertain
428 forced response (Fig. 6a, b). Furthermore, the correlation coefficients between the original rainfall
429 trends ($pr(i)$) and the trends of the internal part ($pr_{internal}(i)$) are 0.78 and 0.99, respectively, for the
430 period of 1950-1999 and 1999-2013 (Fig. 6c, d). The significant correlation coefficients imply that at
431 the regional scale the total spread of rainfall trend is dominated by the uncertainties arising from
432 internal variability during both historical periods. Thus, internal variability can greatly modulate both
433 the decline during 1950-1999 and the recovery during 1999-2013 of ISM rainfall.

434 ***4.2 IPO helps modulate ISM rainfall trends***

435 The PDO/IPO has been shown to have an influence on decadal rainfall variations over India in
436 previous studies (Krishnan and Sugi 2003; Krishnamurthy and Krishnamurthy 2013; Joshi and Pandey
437 2011; Dong and Dai 2015; Joshi and Rai 2015). The observed PDO/IPO experienced a negative-to-
438 positive-to-negative phase evolution during 1950-2013 (Dong and Dai 2015; Joshi and Rai 2015; Dong
439 et al. 2018), as also indicated by an IPO index defined in terms of SST gradients between the tropical
440 central-eastern Pacific (TCEP) and the Northern Pacific (NP) (see Methods; Fig. 2). The switch points
441 are seen around the late 1970s and around 2000 (Fig. 2e). Due to the combined influence of external
442 forcing and internal variability in the observations, the negative correlation between temporal
443 variations of the IPO and NCI rainfall during 1950-2013 is only weak. However, the observed IPO
444 index still shows an increasing trend of $0.66 \text{ K decade}^{-1}$ ($p < 0.01$) during 1950-1999 and a decreasing
445 trend of $-0.37 \text{ K decade}^{-1}$ (p value is 0.11 due to the small number of years) during 1999-2013. Since
446 the negative-to-positive IPO phase transition has been suggested to help explain the 1950-1999 ISM
447 drying trend (Salzmann and Cherian 2015), the positive-to-negative IPO transition afterwards may
448 have a link with the recent wetting trend.

449 To determine whether the IPO evolution helps modulate ISM changes, we used the ESPPE to
450 quantify the principal internal mode responsible for the spread in the rainfall trends. The 57 SST trend
451 patterns derived from ESPPE members are regressed onto the 57 values of internal NCI rainfall trends
452 through the member index during both periods (Fig. 6e, f). This regression method helps identify the
453 dominant internal variability in the ocean related to the trend spread of monsoon rainfall. The results
454 of both periods feature a negative correlation in TCEP and a positive correlation in NP (Fig. 6e, f),
455 which is similar to the observed IPO-like pattern and the internal IPO mode of ESPPE (Fig. 2). To
456 directly confirm the influence of the IPO, we chose the 10 members with the strongest positive IPO

457 phase transitions (Pos10) during 1950-1999 and the 10 members with the strongest negative phase
458 transitions (Neg10) during 1999-2013, respectively (Fig. 2f). The composites of Pos10 and Neg10
459 indeed reproduce a decreasing trend of NCI rainfall over 1950-1999 and an increasing trend afterwards,
460 respectively (Fig. 3n). The differences between the chosen members and the ensemble mean (Pos10-
461 EM or Neg10-EM) suggest that the IPO helps modulate both the ISM decline during 1950-1999 and
462 its recovery over 1999-2013.

463 ***4.3 Physical mechanisms of IPO modulating the decline and recovery of ISM rainfall***

464 Our large ESPPE also offers the opportunity to re-examine how IPO phase transitions help
465 modulate the interdecadal decline and recovery of ISM rainfall in 1950-2013. Through a moisture
466 budget analysis on the rainfall trend difference between the Pos10-EM during 1950-1999 and Neg10-
467 EM during 1999-2013, the dynamic component of moisture convergence appears to play a dominant
468 role in modulating the NCI rainfall (Fig. 7a), which is also shown in its spatial patterns (Fig. 7b-e).
469 Further decomposition of the dynamic component shows that the dominant contributions come from
470 the vertical and zonal moisture convergence (Fig. 7a, f-i). The anomalous vertical moisture
471 convergence covers a wide spatial scale including the Indian subcontinent and adjacent seas (Fig. 7f,
472 g), similar to the anomaly rainfall pattern (Fig. 7b, c), while the zonal moisture convergence shows a
473 bipolar pattern that leading to the rainfall anomalies over northern India (Fig. 7h, i). These results
474 suggest a consistently key role of anomalous vertical motion and zonal moisture advection in
475 modulating both the decline and the recovery of ISM rainfall by the IPO.

476 To investigate the anomalous circulation associated with the IPO phase transitions, we further
477 calculated the composite differences of Pos10-EM in 1950-1999 and Neg10-EM in 1999-2013 (Fig.

478 8). During 1950-1999, warm SST anomalies over the TCEP weaken the Walker circulation (Fig. 8a).
479 The 200hPa velocity potential trend differences of Pos10-EM exhibit a decrease (divergence) over the
480 central-eastern Pacific and an increase (convergence) across 40°E–140°E, especially over the tropical
481 Indian Ocean and Indian subcontinent (Fig. 8a). The upper-level convergence over India and the
482 adjacent seas corresponds to the anomalous descending motion, which suppresses ISM convection and
483 rainfall (Fig. 7f). Meanwhile, the depressed convection over India establishes two anomalous
484 anticyclones to its northwest and southwest asymmetrically (Fig. 8c, e) according to the Matsuno–Gill
485 theory (Matsuno 1966; Gill 1980). The anomalous circulation opposes the climatological monsoon
486 flow over India and weakens the cross-equatorial monsoon circulation (Fig. 8e). The westerlies on the
487 northern flank of the northwest anticyclonic anomalies advect relatively drier air from the Eurasian
488 landmass (Parker et al. 2016) (i.e. Pakistan, Afghanistan) to the west of NCI (Fig. 8e). The dry
489 advection decreases rainfall over northern India via zonal moisture convergence (Fig. 7h). The
490 anomalous low-level westerlies over the tropical central western Pacific and South China Sea (Fig. 8e)
491 associated with the weakened Walker circulation also help to maintain the zonal dry advection from
492 the west (Chen and Zhou 2015).

493 Accompanying the IPO phase shift from positive to negative during 1999-2013, the anomalous
494 circulation shows opposite patterns associated with cold SST anomalies over the TCEP. The Walker
495 circulation is enhanced as indicated by the 200hPa velocity potential trend difference of Neg10-EM
496 (Fig. 8b). The upper-level divergence represents the anomalous ascent over India and the adjacent seas,
497 which enhances ISM convection and rainfall (Fig. 7g). Similarly, the enhanced convection over India
498 establishes two anomalous asymmetric cyclones to its west, leading to the strengthened monsoon
499 circulation (Fig. 8d, f). Easterlies over the northern Indian subcontinent advect relatively wetter air

500 from the Bay of Bengal and Indochina peninsula into the east of NCI (Fig. 8f). The moisture
501 convergence increases rainfall over northern India via positive zonal moisture convergence (Fig. 7i).
502 Furthermore, the anomalous low-level easterlies over the tropical central western Pacific and South
503 China Sea are also evident (Fig. 8f). Our results suggest consistent atmospheric processes related to
504 the IPO appear to work in both directions during the two periods of decline and revival of ISM rainfall.

505 Previous studies have also suggested that the interdecadal variations of ISM rainfall during 1950-
506 2013 are closely related to changes in the meridional thermal contrast extending from the surface to
507 the mid-upper troposphere (Jin and Wang 2017; Roxy 2017). Thus, in addition to the above changes
508 in large-scale circulation, we further show that another mechanism of the IPO helps modulate the
509 interdecadal variations of ISM via influencing the related meridional thermal contrast (Figs. 9-10).

510 Accompanying the positive IPO phase transition during 1950-1999, the trend differences of
511 Pos10-EM exhibit warming SST anomalies over the tropical Indian Ocean (40°E–100°W, 10°S–25°N)
512 and cooling surface temperature over the landmass to the north of India (65°E–90°E, 30°N–45°N) (Fig.
513 9a). The strong surface warming of the Indian subcontinent is consistent with the decreased ISM
514 rainfall in this period (Fig. 8c). From 1999 to 2013, the trend of Neg10-EM shows opposite land-sea
515 surface temperature changes accompanying the IPO phase shift from positive to negative (Fig. 9b). As
516 shown in previous studies (Dong et al. 2016), the IPO has a footprint on decadal SST variations in the
517 Indian Ocean via atmospheric adjustments caused by changing surface heat fluxes, sea surface height
518 and thermocline depth. Meanwhile, the IPO also has a negative correlation with surface temperature
519 in a band across the Mediterranean-Middle East-northern India through anomalous atmospheric
520 circulation (Dong and Dai 2015). The composite surface thermal contrast between the tropical Indian
521 Ocean and the landmass north of India shows a strengthening tendency during 1950-1999, followed

522 by a weakening tendency during 1999-2013, similar to the time variations derived from observations
523 (Fig. 9c). However, the surface temperature over land and the SST of Indian Ocean are at different
524 pressure levels because of local topography. The role of the tropospheric temperature gradients at the
525 same pressure level on ISM variations should be considered (Dai et al. 2013).

526 The vertical wind shear over South Asia has been widely used to define the strength of ISM
527 (Webster and Yang 1992). Considering the thermal wind relationship, similar temperature gradients in
528 the mid-upper layers play a larger role on the vertical wind shear over the ISM region than gradients
529 in the lower troposphere (Dai et al. 2013). Thus, the IPO can affect the ISM more effectively through
530 its influence on the meridional thermal contrast in the mid-upper troposphere (Fig. 10). During 1950-
531 1999, the 500-200hPa tropospheric thickness trend of Pos10-EM increases over the tropical Indian
532 Ocean (60°E–100°E, 10°S–10°N) and decreases over Eurasia (60°E–100°E, 25°N–45°N), while an
533 opposite trend pattern occurs in 1999-2013 for Neg10-EM (Fig. 10a, b). The composite variations of
534 meridional thermal contrast in the troposphere based on Pos10-EM in 1950-1999 and Neg10-EM in
535 1999-2013 feature an increasing trend in the former period and a decreasing trend afterwards (Fig.
536 10c). In response to the SST anomalies over TCEP, the local convective latent heating changes, which
537 then affects the tropical tropospheric temperature and thus the meridional tropospheric temperature
538 gradient over the Indian sector (Chiang and Sobel 2002). Previous studies (Goswami and Xavier 2005;
539 Xavier et al. 2007) have discussed how ENSO-related tropical SST anomalies influence ISM via
540 changes in tropospheric temperatures. Here, we show that IPO-related tropical Pacific SST anomalies
541 can also modulate the ISM on decadal-to-multidecadal time scales through similar processes, thus
542 extending the ENSO-related tropospheric temperature mechanism to a longer time scale. With the
543 detailed investigation of the IPO's dynamical mechanisms showed above, our study helps reconcile

544 different explanations for the recent interdecadal variations in ISM rainfall proposed by previous
545 studies (Krishnamurthy and Krishnamurthy 2013; Roxy et al. 2015; Salzmman and Cherian 2015; Jin
546 and Wang 2017).

547 **5. Adjustments to simulated ISM rainfall trends considering both external forcing** 548 **and observed IPO evolution**

549 Both external forcing and internal variability (with a non-negligible contribution from the IPO)
550 contribute to the recent decline and recovery of ISM rainfall. To further quantify the relative
551 contributions of external forcing and the IPO to the rainfall trends, we applied an ‘adjustment’ method
552 to the 57 ESPPE members to take the observational IPO phase transition into account with the
553 externally-forced change, following Salzmman and Cherian (2015). The raw ESPPE members have
554 different IPO phases due to its random realizations in the freely-run coupled model. The ‘adjustment’
555 method first removes the raw IPO-related rainfall trends and then adds the influence of the observed
556 IPO phase transition through regression within each member (see Methods; Equation (6)-(8)).
557 Compared to the EM without the adjustment (Fig. 3h, k), which represents the response to external
558 forcing only, the EM of the adjusted ESPPE members (Fig. 11b, e) is the combination of the response
559 to external forcing and the influence of the observed IPO phase transition (Fig. 11a, d). Here, the
560 adjustment to the ISM rainfall trend during 1950-1999 also provides a comparison with the results of
561 Salzmman and Cherian (2015), which were derived from the CMIP5 multi-model ensemble.

562 After considering the influence of the observed IPO evolutions, the EM of the adjusted internal
563 part of rainfall derived from ESPPE, representing the rainfall changes caused by the observed IPO
564 transition, shows a strong drying trend over the ISM region during 1950-1999 (Fig. 11a). Meanwhile,

565 it shows an additional wetting trend over India during 1999-2013 (Fig. 11d). In both time periods, the
566 EMs of the adjusted rainfall trends (see Methods; $\partial_t pr_{adj}(i)$), which represent the combined
567 influences of external forcing and the observational IPO phase transition, are close to the observed
568 ISM rainfall trends (Fig. 11b, e).

569 Quantitatively, during 1950-1999, the adjustment considering the observed negative-to-positive
570 IPO transition decreases the NCI rainfall trend from 0.01 ± 0.14 to -0.15 ± 0.13 mm day⁻¹ decade⁻¹ in
571 ESPPE (Fig. 11c), which is comparable to the adjustment from -0.02 ± 0.06 to -0.11 ± 0.08 mm day⁻¹
572 decade⁻¹ derived from the CMIP5 multi-model ensemble by Salzmann and Cherian (2015). The IPO-
573 induced NCI rainfall trend is -0.16 mm day⁻¹ decade⁻¹ in ESPPE during this period. During the revival
574 in 1999-2013, the adjustment increases the simulated NCI rainfall trend from 0.42 ± 0.61 to 0.68 ± 0.54
575 mm day⁻¹ decade⁻¹ (Fig. 11f). Taking the IPO shift from a positive to a negative phase into
576 consideration together with the external forcing, the adjusted NCI rainfall trend is close to the observed
577 wetting trend of 0.66 mm day⁻¹ decade⁻¹, with the IPO-induced trend of 0.26 mm day⁻¹ decade⁻¹.
578 Moreover, the signal-to-noise ratio of rainfall trends among ESPPE members increases from 0.07 to
579 1.15 in 1950-1999 and from 0.69 to 1.26 in 1999-2013; thus, it becomes much higher after the
580 adjustment than before in both time periods. It indicates that the uncertainties in ISM rainfall trends
581 among the 57 members can be narrowed through the adjustments which allow them to have the same
582 observed IPO phase transitions. These results suggest that the adjusted ISM rainfall trends, taking the
583 observed IPO evolution into account as well as the external forcing, becomes close to those observed
584 with a narrowed range of uncertainty. Thus, for effective near-future climate adaptation and mitigation
585 efforts, the IPO's phase transitions must be considered in addition to anthropogenic climate change in
586 South Asia.

587 **6. Comparison of different large ensembles of model simulations**

588 Our results derived from the ESPPE provide a comparison with those from the CMIP5 multi-
589 model ensemble of Salzmänn and Cherian (2015) and Jin and Wang (2017). We further confirmed the
590 results with another 100-member ensemble of simulations based on the MPI-ESM which has been
591 recently completed and made available (Maher et al. 2019). As the largest perturbed-initialization
592 ensemble using a comprehensive climate model, it allows us to directly consider the differences
593 between the individual members as arising from internal variability, without the need for any
594 complicated statistical separation method. The EM of the MPI-ESM also indicates that external forcing
595 partly explains the interdecadal variations of ISM rainfall (Fig. 12a, b), though the forced rainfall trends
596 are quantitatively different from that of the ESPPE (Fig. 3g, k), as expected. The large spread of ISM
597 rainfall trends among ensemble members caused by internal variability is also evident during both
598 periods (Fig. 12c, d). The regression patterns of SST trends with respect to the NCI rainfall trends
599 across the 100 MPI-ESM members confirm that the IPO helps modulate the interdecadal variability of
600 ISM rainfall (Fig. 13a, b). The composites of Pos10 members from 1950-1999 and Neg10 members
601 from 1999-2013 in MPI-ESM ensemble, respectively, also reproduce the recent decline and recovery
602 of ISM rainfall (Fig. 12e-g). Moreover, the adjusted ISM rainfall taking into account the influence of
603 the observed IPO evolution with external forcing shows a decreasing trend during 1950-1999 and an
604 increasing trend during 1999-2013, close to the observations (Fig. 13c-f). This strongly supports our
605 earlier results derived from the ESPPE.

606 **7. Summary and concluding remarks**

607 In this study, we investigated the influence of historical external forcing and internal variability

608 on interdecadal variability of ISM rainfall during 1950-2013 using a 57-member ensemble of ESPPE
609 and a 100-member ensemble of MPI-ESM. We also explored possible physical mechanisms related to
610 the recent drying and subsequent recovery. The main results are summarized in Fig. 14 and given
611 below:

612 **(1) Role of external forcing:** In ESPPE's ensemble mean, an insignificant externally-forced ISM
613 rainfall trend was seen from 1950-1999 followed by a significant increasing trend from 1999-2013.
614 During 1950-1999, atmospheric moisture content increased due to global warming, which
615 enhances ISM rainfall thermodynamically. Dynamically, the zonally nonuniform warming over the
616 tropical Indian Ocean induces anomalous ascent over southern and western India associated with
617 increase local rainfall. Meanwhile, a cooling trend of surface temperature close to the foothills of
618 the Himalayas induces anomalous descent reducing rainfall over northern India. Overall, the
619 competing dynamic and thermodynamic processes appear to result in the overall insignificant
620 rainfall trend. During 1999-2013, atmospheric moisture content continued to increase associated
621 with enhanced global warming. At the same time, dynamic moisture convergence has also
622 strengthened related to enhanced land-sea thermal contrast between East Asia and the western
623 north Pacific Ocean. The accumulative impact of the dynamic and thermodynamic processes
624 results in the increasing ISM trend during this period. As a result, external forcing partly
625 contributes to the observed interdecadal variability of ISM rainfall.

626 **(2) Role of internal variability:** From our analysis, it appeared that neither of the trends of ISM
627 rainfall pre- and post-2000 can be solely explained as a response to external forcing. Internal
628 variability also had a significant role, mainly arising from the IPO. The negative-to-positive-to-
629 negative IPO evolution during 1950-2013 modulates the ISM by inducing anomalous vertical

630 motion and zonal moisture convergence related to an anomalous Walker circulation. The IPO can
631 also influence ISM variability through modulating the meridional thermal contrasts over South
632 Asia. The underlying mechanisms of the IPO in modulating the recent ISM rainfall variability
633 appear to be valid in both directions during the two periods.

634 **(3) Relative contributions of external forcing & internal variability:** Quantitatively, the observed
635 negative-to-positive IPO phase transition during 1950-1999 induced a negative NCI rainfall of -
636 0.16 mm day⁻¹ decade⁻¹, which decreased the externally-forced rainfall trend from 0.01 to -0.15
637 mm day⁻¹ decade⁻¹. During 1999-2013, the positive-to-negative IPO transition caused a positive
638 NCI rainfall trend of 0.26 mm day⁻¹ decade⁻¹, which increased the forced trend of 0.42 to 0.68 mm
639 day⁻¹ decade⁻¹. The ensemble mean of the adjusted rainfall trends ($\partial_t pr_{adj}(i)$), which represent the
640 combined influences of external forcing and the observational IPO phase transition, are close to
641 the observed rainfall trends of -0.11 and 0.68 mm day⁻¹ decade⁻¹ pre- and post-2000, respectively.
642 Moreover, the signal-to-noise ratios have also become greater after the adjustment, indicating that
643 the uncertainties in ISM rainfall trends among the ensemble members are reduced after modifying
644 their IPO phase transitions to match those of observations.

645 **(4) Comparison of different ensembles:** We also verified the results with a second ensemble of 100
646 simulations based on the MPI-ESM. Differences were found in the quantitative rainfall trends
647 caused by external forcing between the two ensembles. However, the MPI-ESM ensemble supports
648 the main results given by the ESPPE that the IPO helps modulate the recent decline and recovery
649 of ISM rainfall. By adjusting the simulated rainfall trends, according to the observed IPO phase
650 transition, both ensembles successfully reproduced the observed decline in 1950-1999 and the
651 recovery afterwards.

652 In summary, our study implies the roles of both external forcing and internal variability in the
653 observed variability of ISM rainfall, with the IPO identified as a contributing internal mode. We also
654 analysed the physical processes through which external forcing and the IPO modulate the ISM,
655 respectively. Our results reveal, for the first time, the linkage between and consistency among different
656 explanations of the decadal-to-multidecadal variations in ISM rainfall proposed in the literature
657 (Goswami and Xavier 2005; Xavier et al. 2007; Krishnamurthy and Krishnamurthy 2013; Salzmann
658 and Cherian 2015; Jin and Wang 2017). Our findings also pose a new perspective for future projections
659 of ISM, that the phase transitions of the IPO must be considered in addition to the response to external
660 forcing.
661

662 **Acknowledgements**

663 This work was supported by the Strategic Priority Research Program of the Chinese Academy of
664 Sciences under Grant No. XDA20060102 and the International Partnership Program of Chinese
665 Academy of Sciences under Grant No. 134111KYSB20160031. AGT was supported by the REAL
666 Projections and EMERGENCE projects (NERC grant numbers NE/N018591/1 and NE/S004890/1
667 respectively). A. Dai was also supported by the National Science Foundation (OISE-1743738), and
668 the U.S. National Oceanic and Atmospheric Administration (NA15OAR4310086 and
669 NA18OAR4310425). RC, JM and JR were supported by the UK-China Research and Innovation
670 Partnership Fund through the Met Office Climate Science for Service Partnership (CSSP) China as
671 part of the Newton Fund. We acknowledge that the 57-member Earth system perturbed parameter
672 ensemble (ESPPE) simulations with the HadCM3C model were run by Hugo Lambert and Ben Booth
673 at the UK Met Office. The ESPPE data is available from the UK Met Office for non-commercial use.
674 Requests for ESPPE data should be addressed to Dr. James M. Murphy (email:
675 james.murphy@metoffice.gov.uk). The historical simulations of MPI-ESM ensemble were performed
676 with the Swiss National Computing Centre (CSCS) and the corresponding RCP scenarios simulations
677 were performed with the facilities at the German Climate Computing Centre (DKRZ). The MPI-ESM
678 grand ensemble data is available for non-commercial use via [https://esgf-data.dkrz.de/projects/mipi-](https://esgf-data.dkrz.de/projects/mipi-ge/)
679 [ge/](https://esgf-data.dkrz.de/projects/mipi-ge/). Detailed information of the data and references can be found from the website:
680 <https://www.mpimet.mpg.de/en/grand-ensemble/>. The observational rainfall and surface temperature
681 datasets are available on the Climate Data Guide website (<https://climatedataguide.ucar.edu>). The
682 NCEP/NCAR reanalysis dataset can be obtained from <https://www.esrl.noaa.gov/psd>. The published
683 PDO index of Mantua and Hare (2002) is available from the University of Washington, USA

684 (<http://www.jisao.washington.edu/pdo>). The published TPI index of Henley et al. (2015) was accessed
685 at <https://www.esrl.noaa.gov/psd/data/timeseries/IPOTPI>. We also acknowledge the support from
686 Jiangsu Collaborative Innovation Center for Climate Change.

687

688 **References**

- 689 Annamalai, H., K. Hamilton, and K. R. Sperber, 2007: The South Asian Summer Monsoon and Its
690 Relationship with ENSO in the IPCC AR4 Simulations. *Journal of Climate*, 20, 1071-1092.
691 doi:10.1175/jcli4035.1
- 692 Annamalai, H., J. Hafner, K. P. Sooraj, and P. Pillai, 2013: Global Warming Shifts the Monsoon
693 Circulation, Drying South Asia. *Journal of Climate*, 26, 2701-2718. doi:10.1175/jcli-d-12-
694 00208.1
- 695 Bollasina, M. A., Y. Ming, and V. Ramaswamy, 2011: Anthropogenic aerosols and the weakening of
696 the South Asian summer monsoon. *Science*, 334, 502-505. doi:10.1126/science.1204994
- 697 Chen, X. L., and T. J. Zhou, 2015: Distinct effects of global mean warming and regional sea surface
698 warming pattern on projected uncertainty in the South Asian summer monsoon. *Geophysical*
699 *Research Letters*, 42, 9433-9439. doi:10.1002/2015gl066384
- 700 Chiang, J. C. H., and A. H. Sobel, 2002: Tropical tropospheric temperature variations caused by ENSO
701 and their influence on the remote tropical climate. *Journal of Climate*, 15, 2616-2631.
702 doi:10.1175/1520-0442(2002)015<2616:ttvcb>2.0.co;2
- 703 Chou, C., and J. D. Neelin, 2004: Mechanisms of global warming impacts on regional tropical
704 precipitation. *Journal of Climate*, 17, 2688-2701. doi:10.1175/1520-
705 0442(2004)017<2688:mogwio>2.0.co;2
- 706 Chou, C., J. D. Neelin, C.-A. Chen, and J.-Y. Tu, 2009: Evaluating the “Rich-Get-Richer” Mechanism
707 in Tropical Precipitation Change under Global Warming. *Journal of Climate*, 22, 1982-2005.
708 doi:10.1175/2008jcli2471.1
- 709 Chou, C., D. Ryu, M. Lo, H. Wey, and H. Malano, 2018: Irrigation-induced land-atmosphere feedbacks
710 and their impacts on Indian summer monsoon. *Journal of Climate*, 31, 8785-8801.
- 711 Collins, M., R. Knutti, J. Arblaster, J. L. Dufresne, T. Fichet, P. Friedlingstein, et al., 2013: Long-
712 term climate change: projections, commitments and irreversibility. In: Stocker, T. F., D. Qin,
713 G. K. Plattner, M. Tignor, S. K. Allen, J. Boschung, et al., editors. *Climate change 2013: The*
714 *physical science basis*. Cambridge: Contribution of working group I to the Fifth Assessment
715 Report of the Intergovernmental Panel on Climate Change, pp. 1029–136.
- 716 Dai, A., and C. E. Bloecker, 2019: Impacts of internal variability on temperature and precipitation
717 trends in large ensemble simulations by two climate models. *Climate Dynamics*, 52, 289-306.
- 718 Dai, A., J. C. Fyfe, S.-P. Xie, and X. Dai, 2015: Decadal modulation of global surface temperature by
719 internal climate variability. *Nature Climate Change*, 5, 555-559. doi:10.1038/nclimate2605.
- 720 Dai, A., H. Li, Y. Sun, L. Hong, Linho, C. Chou, and T. Zhou, 2013: The relative roles of upper and
721 lower tropospheric thermal contrasts and tropical influences in driving Asian summer
722 monsoons. *Journal of Geophysical Research*, 118, 7024-7045.
- 723 Deser, C., R. Knutti, S. Solomon, and A. S. Phillips, 2012: Communication of the role of natural
724 variability in future North American climate. *Nature Climate Change*, 2, 775-779.
725 doi:10.1038/nclimate1562

- 726 Dong, B., and A. Dai, 2015: The influence of the Interdecadal Pacific Oscillation on Temperature and
727 Precipitation over the Globe. *Climate Dynamics*, 45, 2667-2681. doi:10.1007/s00382-015-
728 2500-x
- 729 Dong, B., A. Dai, M. Vuille, and O. Elison Timm, 2018: Asymmetric modulation of ENSO
730 teleconnections by the Interdecadal Pacific Oscillation. *J. Climate*, 31:7337-7361.
731 <https://doi.org/10.1175/JCLI-D-17-0663.1>.
- 732 Dong, L., and T. Zhou, 2014: The Indian Ocean Sea Surface Temperature Warming Simulated by
733 CMIP5 Models during the Twentieth Century: Competing Forcing Roles of GHGs and
734 Anthropogenic Aerosols. *Journal of Climate*, 27, 3348-3362. doi:10.1175/jcli-d-13-00396.1
- 735 Dong, L., T. Zhou, and X. Chen, 2014: Changes of Pacific decadal variability in the twentieth century
736 driven by internal variability, greenhouse gases, and aerosols. *Geophysical Research Letters*,
737 41, 8570-8577. doi:10.1002/2014gl062269
- 738 Dong, L., T. Zhou, A. Dai, F. Song, B. Wu, and X. Chen, 2016: The Footprint of the Inter-decadal
739 Pacific Oscillation in Indian Ocean Sea Surface Temperatures. *Scientific Reports*, 6.
740 doi:10.1038/srep21251
- 741 Frankcombe, L. M., M. H. England, M. E. Mann, and B. A. Steinman, 2015: Separating Internal
742 Variability from the Externally Forced Climate Response. *Journal of Climate*, 28, 8184-8202.
743 doi:10.1175/jcli-d-15-0069.1
- 744 Gadgil, S., 2003: THE INDIAN MONSOON AND ITS VARIABILITY. *Annual Review of Earth and*
745 *Planetary Sciences*, 31, 429-467.
- 746 Gill, A. E., 1980: Some simple solutions for heat - induced tropical circulation. *Quarterly Journal of*
747 *the Royal Meteorological Society*, 106, 447-462.
- 748 Gordon, C., and Coauthors, 2000: The simulation of SST, sea ice extents and ocean heat transports in
749 a version of the Hadley Centre coupled model without flux adjustments. *Climate Dynamics*,
750 16, 147-168. doi:10.1007/s003820050010
- 751 Goswami, B. N., and P. K. Xavier, 2005: ENSO control on the south Asian monsoon through the length
752 of the rainy season. *Geophysical Research Letters*, 32. doi:10.1029/2005gl023216
- 753 Goswami, B. N., V. Venugopal, D. Sengupta, M. S. Madhusoodanan, and P. K. Xavier, 2006:
754 Increasing trend of extreme rain events over India in a warming environment. *Science*, 314,
755 1442-1445. doi:10.1126/science.1132027
- 756 Guo, L., A. G. Turner, and E. J. Highwood, 2015: Impacts of 20th century aerosol emissions on the
757 South Asian monsoon in the CMIP5 models. *Atmospheric Chemistry and Physics*, 15, 6367-
758 6378. doi:10.5194/acp-15-6367-2015
- 759 Harris, I., P. D. Jones, T. J. Osborn, and D. H. Lister, 2014: Updated high-resolution grids of monthly
760 climatic observations - the CRU TS3.10 Dataset. *International Journal of Climatology*, 34, 623-
761 642. doi:10.1002/joc.3711
- 762 Hawkins, E., and R. Sutton, 2009: The Potential to Narrow Uncertainty in Regional Climate
763 Predictions. *Bulletin of the American Meteorological Society*, 90, 1095-1108.

- 764 doi:10.1175/2009bams2607.1
- 765 ———, 2010: The potential to narrow uncertainty in projections of regional precipitation change.
766 *Climate Dynamics*, 37, 407-418. doi:10.1007/s00382-010-0810-6
- 767 Henley, B. J., J. Gergis, D. J. Karoly, S. Power, J. Kennedy, and C. K. Folland, 2015: A Tripole Index
768 for the Interdecadal Pacific Oscillation. *Climate Dynamics*, 45, 3077-3090.
769 doi:10.1007/s00382-015-2525-1
- 770 Hua, W., A. Dai, and M. Qin, 2018: Contributions of Internal Variability and External Forcing to the
771 Recent Pacific Decadal Variations. *Geophysical Research Letters*, 45, 7084-7092.
772 doi:10.1029/2018gl079033
- 773 Huang, X., T. Zhou, W. Zhang, J. Jiang, P. Li, and Y. Zhao, 2019: Northern Hemisphere land monsoon
774 precipitation changes in the twentieth century revealed by multiple reanalysis datasets. *Climate*
775 *Dynamics*, 1-19. doi: 10.1007/s00382-019-04982-z
- 776 Jiang, J., and T. Zhou, 2019: Global monsoon responses to decadal sea surface temperature variations
777 during the 20th century: Evidence from AGCM simulations. *Journal of Climate*, online
778 published. doi: 10.1175/JCLI-D-18-0890.1
- 779 Jiang, X., and M. Ting, 2017: A Dipole Pattern of Summertime Rainfall across the Indian Subcontinent
780 and the Tibetan Plateau. *Journal of Climate*, 30, 9607-9620.
- 781 Jin, Q., and C. Wang, 2017: A revival of Indian summer monsoon rainfall since 2002. *Nature Climate*
782 *Change*, 7, 587-594. doi:10.1038/nclimate3348
- 783 Jin, Q., Z.-L. Yang, and J. Wei, 2016: Seasonal Responses of Indian Summer Monsoon to Dust
784 Aerosols in the Middle East, India, and China. *Journal of Climate*, 29, 6329-6349.
785 doi:10.1175/jcli-d-15-0622.1
- 786 Jones, P. D., D. H. Lister, T. J. Osborn, C. Harpham, M. Salmon, and C. P. Morice, 2012: Hemispheric
787 and large-scale land-surface air temperature variations: An extensive revision and an update to
788 2010. *Journal of Geophysical Research-Atmospheres*, 117. doi:10.1029/2011jd017139
- 789 Joshi, M. K., and F. Kucharski, 2017: Impact of Interdecadal Pacific Oscillation on Indian summer
790 monsoon rainfall: an assessment from CMIP5 climate models. *Climate Dynamics*, 48, 2375-
791 2391. doi:10.1007/s00382-016-3210-8
- 792 Joshi, M. K., and A. C. Pandey, 2011: Trend and spectral analysis of rainfall over India during 1901–
793 2000. *Journal of Geophysical Research*, 116, D06104. doi: 10.1029/2010JD014966
- 794 Joshi, M. K., and A. Rai, 2015: Combined interplay of the Atlantic multidecadal oscillation and the
795 interdecadal Pacific oscillation on rainfall and its extremes over Indian subcontinent. *Climate*
796 *Dynamics*, 44, 3339-3359. doi: 10.1007/s00382-014-2333-z
- 797 Kalnay, E., and Coauthors, 1996: The NCEP/NCAR 40-year reanalysis project. *Bulletin of the*
798 *American Meteorological Society*, 77, 437-471. doi:10.1175/1520-
799 0477(1996)077<0437:tnyrp>2.0.co;2
- 800 Kendall, M., G. 1975: Rank Correlation Methods. 4th Edition, Charles Griffin, London.

- 801 Kitoh, A., H. Endo, K. Krishna Kumar, I. F. A. Cavalcanti, P. Goswami, and T. Zhou, 2013: Monsoons
802 in a changing world: A regional perspective in a global context. *Journal of Geophysical*
803 *Research: Atmospheres*, 118, 3053-3065. doi:10.1002/jgrd.50258
- 804 Krishnamurthy, L., and V. Krishnamurthy, 2013: Influence of PDO on South Asian summer monsoon
805 and monsoon–ENSO relation. *Climate Dynamics*, 42, 2397-2410. doi:10.1007/s00382-013-
806 1856-z
- 807 Krishnan, R., and M. Sugi, 2003: Pacific decadal oscillation and variability of the Indian summer
808 monsoon rainfall. *Climate Dynamics*, 21, 233-242. doi:10.1007/s00382-003-0330-8
- 809 Lambert, F. H., G. R. Harris, M. Collins, J. M. Murphy, D. M. H. Sexton, and B. B. Booth, 2013:
810 Interactions between perturbations to different Earth system components simulated by a fully-
811 coupled climate model. *Climate Dynamics*, 41, 3055-3072. doi:10.1007/s00382-012-1618-3
- 812 Li, L., W. Li, and A. P. Barros, 2013: Atmospheric moisture budget and its regulation of the summer
813 precipitation variability over the Southeastern United States. *Climate Dynamics*, 41, 613-631.
814 doi:10.1007/s00382-013-1697-9
- 815 Li, X., M. Ting, C. Li, and N. Henderson, 2015: Mechanisms of Asian Summer Monsoon Changes in
816 Response to Anthropogenic Forcing in CMIP5 Models. *Journal of Climate*, 28, 4107-4125.
817 doi:10.1175/jcli-d-14-00559.1
- 818 Liu, H., T. Zhou, Y. Zhu, Y. Lin, 2012: The strengthening East Asia summer monsoon since the early
819 1990s. *Chinese Science Bulletin*, 57, 1553-1558. doi:10.1007/s11434-012-4991-8
- 820 Maher, N., D. Matei, S. Milinski, and J. Marotzke, 2018: ENSO Change in Climate Projections: Forced
821 Response or Internal Variability? *Geophysical Research Letters*, 45, 11390-11398.
822 doi:10.1029/2018gl079764
- 823 Maher, N., and Coauthors, 2019: The Max Planck Institute Grand Ensemble-Enabling the Exploration
824 of Climate System Variability. *Journal of Advances in Modeling Earth Systems*, 11, 2050-2069.
- 825 Mann, H. B., 1945: NONPARAMETRIC TESTS AGAINST TREND. *Econometrica*, 13, 245-259.
826 doi:10.2307/1907187
- 827 Mantua, N. J., and S. R. Hare, 2002: The Pacific decadal oscillation. *Journal of Oceanography*, 58, 35-
828 44. doi:10.1023/a:1015820616384
- 829 Matsuno, T., 1966: Quasi-Geostrophic Motions in the Equatorial Area. *Journal of The Meteorological*
830 *Society of Japan*, 44, 25-43.
- 831 May, W., 2010: The sensitivity of the Indian summer monsoon to a global warming of 2°C with respect
832 to pre-industrial times. *Climate Dynamics*, 37, 1843-1868. doi:10.1007/s00382-010-0942-8
- 833 Murphy, J. M., D. M. H. Sexton, D. N. Barnett, G. S. Jones, M. J. Webb, and D. A. Stainforth, 2004:
834 Quantification of modelling uncertainties in a large ensemble of climate change simulations.
835 *Nature*, 430, 768-772. doi:10.1038/nature02771
- 836 Murphy, J. M., B. B. Booth, C. A. Boulton, R. T. Clark, G. R. Harris, J. A. Lowe, and D. M. H. Sexton,
837 2014: Transient climate changes in a perturbed parameter ensemble of emissions-driven earth

- 838 system model simulations. *Climate Dynamics*, 43, 2855-2885. doi:10.1007/s00382-014-2097-
839 5
- 840 Parker, D. J., and Coauthors, 2016: The interaction of moist convection and mid-level dry air in the
841 advance of the onset of the Indian monsoon. *Quarterly Journal of the Royal Meteorological*
842 *Society*, 142, 2256-2272. doi:10.1002/qj.2815
- 843 Paul, S., S. Ghosh, R. Oglesby, A. Pathak, A. Chandrasekharan, and R. Ramsankaran, 2016:
844 Weakening of Indian Summer Monsoon Rainfall due to Changes in Land Use Land Cover. *Sci*
845 *Rep*, 6, 32177. doi:10.1038/srep32177
- 846 Rayner, N. A., and Coauthors, 2003: Global analyses of sea surface temperature, sea ice, and night
847 marine air temperature since the late nineteenth century. *Journal of Geophysical Research-*
848 *Atmospheres*, 108. doi:10.1029/2002jd002670
- 849 Roxy, M. K., 2017: Land warming revives monsoon. *Nature Climate Change*, 7, 549-550.
850 doi:10.1038/nclimate3356
- 851 Roxy, M. K., K. Ritika, P. Terray, R. Murtugudde, K. Ashok, and B. N. Goswami, 2015: Drying of
852 Indian subcontinent by rapid Indian Ocean warming and a weakening land-sea thermal gradient.
853 *Nat Commun*, 6, 7423. doi:10.1038/ncomms8423
- 854 Saha, A., S. Ghosh, A. S. Sahana, and E. P. Rao, 2014: Failure of CMIP5 climate models in simulating
855 post-1950 decreasing trend of Indian monsoon. *Geophysical Research Letters*, 41, 7323-7330.
856 doi:10.1002/2014gl061573
- 857 Salzmann, M., and R. Cherian, 2015: On the enhancement of the Indian summer monsoon drying by
858 Pacific multidecadal variability during the latter half of the twentieth century. *Journal of*
859 *Geophysical Research: Atmospheres*, 120, 9103-9118. doi:10.1002/2015jd023313
- 860 Salzmann, M., H. Weser, and R. Cherian, 2014: Robust response of Asian summer monsoon to
861 anthropogenic aerosols in CMIP5 models. *Journal of Geophysical Research: Atmospheres*, 119,
862 11,321-311,337. doi:10.1002/2014jd021783
- 863 Schneider, U., A. Becker, P. Finger, A. Meyer-Christoffer, M. Ziese, and B. Rudolf, 2014: GPCC's new
864 land surface precipitation climatology based on quality-controlled in situ data and its role in
865 quantifying the global water cycle. *Theoretical and Applied Climatology*, 115, 15-40.
866 doi:10.1007/s00704-013-0860-x
- 867 Seager, R., N. Naik, and G. A. Vecchi, 2010: Thermodynamic and Dynamic Mechanisms for Large-
868 Scale Changes in the Hydrological Cycle in Response to Global Warming. *Journal of Climate*,
869 23, 4651-4668. doi:10.1175/2010jcli3655.1
- 870 Singh, D., S. Ghosh, M. K. Roxy, and S. McDermid, 2019: Indian summer monsoon: Extreme events,
871 historical changes, and role of anthropogenic forcings. *Wiley Interdisciplinary Reviews-*
872 *Climate Change*, 10. doi:10.1002/wcc.571
- 873 Taylor, K. E., R. J. Stouffer, and G. A. Meehl, 2012: AN OVERVIEW OF CMIP5 AND THE
874 EXPERIMENT DESIGN. *Bulletin of the American Meteorological Society*, 93, 485-498.
875 doi:10.1175/bams-d-11-00094.1

- 876 Turner, A. G., and H. Annamalai, 2012: Climate change and the South Asian summer monsoon. *Nature*
877 *Climate Change*, 2, 587-595. doi:10.1038/nclimate1495
- 878 Wang, B., J. Liu, H. J. Kim, P. J. Webster, S. Y. Yim, and B. Xiang, 2013: Northern Hemisphere
879 summer monsoon intensified by mega-El Nino/southern oscillation and Atlantic multidecadal
880 oscillation. *Proc Natl Acad Sci U S A*, 110, 5347-5352. doi:10.1073/pnas.1219405110
- 881 Wang, P. X., B. Wang, H. Cheng, J. Fasullo, Z. Guo, T. Kiefer, and Z. Liu, 2017: The global monsoon
882 across time scales: Mechanisms and outstanding issues. *Earth-Science Reviews*, 174, 84-121.
883 doi:10.1016/j.earscirev.2017.07.006
- 884 Webster, P. J., and S. Yang, 1992: MONSOON AND ENSO - SELECTIVELY INTERACTIVE
885 SYSTEMS. *Quarterly Journal of the Royal Meteorological Society*, 118, 877-926.
886 doi:10.1002/qj.49711850705
- 887 Willmott, C. J., and K. Matsuura, 2000: Terrestrial air temperature and precipitation: Monthly and
888 annual climatologies. Centre for Climate Research, Department of Geography, University of
889 Delaware.
890 [http://climate.geog.udel.edu/~climate/html_pages/Global2_Clim/README.global2_clim.ht](http://climate.geog.udel.edu/~climate/html_pages/Global2_Clim/README.global2_clim.html)
891 [ml](http://climate.geog.udel.edu/~climate/html_pages/Global2_Clim/README.global2_clim.html).
- 892 Xavier, P. K., C. Marzin, and B. N. Goswami, 2007: An objective definition of the Indian summer
893 monsoon season and a new perspective on the ENSO-monsoon relationship. *Quarterly Journal*
894 *of the Royal Meteorological Society*, 133, 749-764. doi:10.1002/qj.45
- 895 Xie, S. P., C. Deser, G. A. Vecchi, J. Ma, H. Teng, and A. T. Wittenberg, 2010: Global warming pattern
896 formation: Sea surface temperature and rainfall. *J. Clim.*, 23, 966-986,
897 doi:10.1175/2009JCLI3329.1.

898 **Figures Caption List**

899

900 **Fig. 1.** Evaluation of the ESPPE and MPI-ESM in simulating climatological June-July-August (JJA) Indian summer
901 monsoon (ISM) rainfall and its relation to IPO. (a) CRU, (c) GPCC, (e) UDel, (g) ESPPE ensemble mean and (i)
902 MPI-ESM ensemble mean (EM) climatological JJA mean rainfall over ISM region in 1950-2013. Regressed 9-year
903 running mean JJA rainfall with respect to the observed IPO index during 1950-2013: (b) CRU, (d) GPCC and
904 (f) UDel. (d) ESPPE and (f) MPI-ESM EM of the regressed internal component of JJA 9-year running mean
905 rainfall onto the IPO index within each ensemble member during 1950-2013. Stippling denotes 4 of 5 ensemble
906 members agreeing on the sign of change. Units: mm day⁻¹.

907

908

909 **Fig. 2.** Regressed 9-year running-mean JJA SST anomalies from HadISST (units: K) with respect to standardized 9-
910 year running-mean (a) PDO index, (b) TPI index and (c) IPO index during the period of 1920-2013. (d) ESPPE EM
911 of regressed 9-year running mean JJA SST with respect to standardized IPO index within each member during the
912 period of 1920-2013. Slant hatching denotes regional signals significant at the 95% confidence level. Stippling
913 denotes 4 of the 5 ensemble members in agreement on the sign of change. (e) Standardized time series of observed
914 IPO index (defined as 9-year running-mean SST gradients between TCEP and NP, positive in red and negative in
915 blue), standardized 9-year running-mean PDO (orange) and TPI (grey) index. The correlation coefficients between
916 the IPO and PDO or TPI indexes are 0.93 and 0.89 ($p < 0.01$), respectively, during the historical period of 1920-
917 2013. (f) Time series of IPO index from different ESPPE members. Black, brown and blue lines denote the IPO
918 indices derived from HadISST observations and the 10 members with the strongest positive (Pos10) and the strongest
919 negative (Neg10) transitions, respectively. The 10 members are chosen separately for both periods of 1950-1999 and
920 1999-2013. Light brown and blue shadings show the spread among the 10 members.

921

922

923 **Fig. 3.** Spatial patterns of 9-year running-mean JJA rainfall trends during the period of 1950-1999 derived from the
924 (a) CRU, (b) GPCC, (c) UDel, (g) the average OBS and (h) the ESPPE EM. (i) The standard deviation (STD) of the
925 rainfall trends among the 57 ESPPE members for 1950-1999. (d, e, f, j, k, l) are same as (a, b, c, g, h, i) but for 1999-
926 2013. Units: mm day⁻¹ decade⁻¹. Slant hatching denotes rainfall trends significant at the 95% confidence level. (m-n)

927 Time series of the 9-year running-mean JJA rainfall anomalies relative to 1950-2013 mean average over north-central
928 India (NCI; 20°N–28°N, 76°E–87°E) outlined by the rectangle in (a-l). Units: mm day⁻¹. In (m), colours of orange,
929 purple, green and black represent the CRU, GPCC, UDel datasets and their average (referred to as OBS), respectively.
930 The coloured numbers in (m) denote the NCI rainfall trends of corresponding datasets during both periods. In (n),
931 black is for the OBS. Red line and shading denote the EM and 5th and 95th percentile of the 57 members. Brown and
932 blue solid lines represent the mean of 10 members with strongest positive (Pos10) and the strongest negative (Neg10)
933 IPO transitions during 1950-1999 and 1999-2013, respectively. Brown and blue dashed lines represent the mean
934 difference of the Pos10 minus EM during 1950-1999 and the Neg10 minus EM during 1999-2013.

935

936

937 **Fig. 4.** Moisture budget analysis of the external forced rainfall trend derived from the ESPPE EM. (a). Moisture
938 budget analysis on EM NCI rainfall trend (dots denote trend differences significant at 95% confidence level) during
939 1950-1999 (dark color bars) and 1999-2013 (light color bars). Rainfall change is balanced by the changes of
940 evaporation, dynamic and thermodynamic components and a nonlinear term (blue and light blue bars). The dynamic
941 component is further separated into vertical, zonal and meridional dynamic components of moisture convergence
942 (red and pink bars). (b, d, f, h) are spatial patterns of EM trend during 1950-1999 of dynamic component,
943 thermodynamic component, vertical dynamic component and zonal dynamic component of moisture advection,
944 respectively. (c, e, g, i) are same as (b, d, f, h) but for 1999-2013. Units: mm day⁻¹ decade⁻¹. Slant hatching denotes
945 regions significant at 95% confidence level.

946

947

948 **Fig. 5.** (a) Trend of EM JJA 850hPa specific humidity (shading, units: g kg⁻¹ decade⁻¹) and EM climatological 850hPa
949 winds (vectors, units: m s⁻¹) from 1950-1999. (c) EM climatological JJA 850hPa specific humidity (shading, units: g
950 kg⁻¹) and trend of EM rainfall (contours, positive in solid blue lines and negative in dashed brown lines; units: mm
951 day⁻¹ decade⁻¹) and 850hPa winds (vectors, units: m s⁻¹ decade⁻¹) from 1950-1999. (e) Trend of EM JJA near surface
952 temperature and SST (shading, units: K decade⁻¹) and sea level pressure (contours, positive in solid purple lines and
953 negative in dashed cyan lines; units: Pa decade⁻¹). (g) Cross section of zonally-averaged (65°E–95°E) trend of EM
954 air temperature (shading, units: K decade⁻¹) and winds (vectors, meridional and vertical components; units: m s⁻¹
955 decade⁻¹). The vertical component is calculated with a scale factor of -100 to allow the vertical pressure-velocity to

956 be comparable with the meridional component. (b, d, f, h) are same as (a, c, e, g) but for 1999-2013. Slant hatching
957 denotes regions significant at 95% confidence level.

958

959

960 **Fig. 6.** Histograms of spread in NCI rainfall trends among 57 members during (a) 1950-1999 and (b) 1999-2013
961 (grey, yellow and blue bars denote the trends of the original rainfall, the internal component and the uncertain-forced
962 component of rainfall). Correlation between trends of the original rainfall (\bar{x} , units: $\text{mm day}^{-1} \text{decade}^{-1}$) and the
963 internal component of the rainfall (\bar{y} , units: $\text{mm day}^{-1} \text{decade}^{-1}$) over the NCI region derived from ESPPE
964 members (number indicated in the circle) during the period (c) 1950-1999 and (d) 1999-2013. (The outlined member
965 “37” in c. is caused by the combination of a positive internal rainfall trend and an evidently positive forced trend.)
966 Brown circles in (c) denote the 10 members with the strongest positive IPO phase transition during 1950-1999. Blue
967 circles in (d) denote the 10 members with the strongest negative IPO phase transition during 1999-2013. The
968 regression pattern of the internal SST trends with respect to the NCI rainfall trends across 57 members through the
969 member index: (e) 1950-1999 and (f) 1999-2013 (units: $\text{K} (\text{decade})^{-1}$). Slant hatching denotes regions significant at
970 the 95% confidence level. The rectangles in (e-f) outline the tropical central-eastern Pacific (TCEP, 170°W – 90°W ,
971 10°S – 10°N) and the North Pacific (NP, 150°E – 150°W , 25°N – 45°N).

972

973

974 **Fig. 7.** Moisture budget analysis of the rainfall trend related to IPO phase transitions. (a). Moisture budget analysis
975 on NCI rainfall trend difference between the 10 members with the strongest positive IPO phase transition and
976 ensemble mean during 1950-1999 (Pos10-EM; dark colour bars). Light colour bars are for Neg10-EM during 1999-
977 2013. Dots denote trend differences significant at 95% confidence level. Rainfall change is balanced by the changes
978 of evaporation, dynamic and thermodynamic components and a nonlinear term (blue and light blue bars). The
979 dynamic component is further separated into vertical, zonal and meridional dynamic components of moisture
980 advection (red and pink bars). (b, d, f, h) are spatial patterns of Pos10-EM trend during 1950-1999 of rainfall, dynamic
981 component, vertical dynamic component and zonal dynamic component of moisture advection, respectively. (c, e, g,
982 i) are same as (b, d, f, h) but for Neg10-EM during 1999-2013. Units: $\text{mm day}^{-1} \text{decade}^{-1}$. Slant hatching denotes
983 regions significant at 95% confidence level.

984

985

986 **Fig. 8.** Mechanisms of IPO's modulation of ISM rainfall reduction and revival. JJA trend differences between the 10
987 members with the strongest positive IPO phase transition and ensemble mean (Pos10-EM) from 1950-1999 for: (a)
988 velocity potential (shading, units: $\text{m}^2 \text{s}^{-1} \text{decade}^{-1}$) and divergent winds (vectors, units: $\text{m s}^{-1} \text{decade}^{-1}$) at 200hPa; (c)
989 rainfall (shading, units: $\text{mm day}^{-1} \text{decade}^{-1}$) and 850hPa stream function anomalies (contours, units: $10^6 \text{m}^2 \text{s}^{-1} \text{decade}^{-1}$);
990 (e) 850hPa winds (vectors, units: $\text{m s}^{-1} \text{decade}^{-1}$) and climatological specific humidity (shading, units: g/kg). (b),
991 (d) and (f) are the same as (a), (c) and (e) but for Neg10-EM trend differences in 1999-2013. Slant hatching denotes
992 regions significant at 95% confidence level.

993

994

995 **Fig. 9.** JJA surface temperature trend related to IPO phase transitions. (a) Spatial patterns of the trend differences of
996 the JJA surface temperature between the 10 members with the strongest positive IPO phase transition and ensemble
997 mean (Pos10-EM) during 1950-1999. (b) is the same as (a) but for trend differences of Neg10-EM during 1999-2013.
998 (c) Composite 9-year running mean anomalies (relative to 1950-2013 mean) derived from the Pos10-EM composite
999 difference for 1950-1999 and the Neg10-EM composite difference for 1999-2013 for surface air temperature over
1000 the landmass north of India (red, land area in 30°N – 45°N , 65°E – 90°E), SST over the tropical Indian Ocean (blue,
1001 ocean area over the 10°S – 25°N , 40°E – 100°E) and the land-sea thermal contrast (black, i.e., the difference between
1002 the red and blue lines). The purple line denotes the observed land-sea surface thermal contrast derived from the
1003 CRUTEM4 and HadISST datasets.

1004

1005

1006 **Fig. 10.** JJA mid-upper tropospheric thickness trend related to IPO phase transitions. (a) Spatial patterns of the trend
1007 differences of the JJA 500-200hPa tropospheric thickness between the 10 members with the strongest positive and
1008 the ensemble mean (Pos10-EM) during 1950-1999. (b) is the same as (a) but for trend differences of Neg10-EM
1009 during 1999-2013. (c) Composite 9-year running mean anomalies (relative to 1950-2013 mean) derived from the
1010 Pos10-EM composite difference for 1950-1999 and the Neg10-EM composite difference for 1999-2013 for 500-
1011 200hPa tropospheric thickness over Eurasia (brown, the northern box over 25°N – 45°N , 60°E – 100°E in a-b), the

1012 tropical Indian Ocean (green, the southern box over 10°S–10°N, 60°E–100°E in a-b) and the meridional thermal
1013 gradient over India (black, i.e., the difference between the brown and green lines). The purple line denotes the
1014 meridional 500-200hPa tropospheric thickness gradient derived from the NCEP/NCAR reanalysis.

1015

1016

1017 **Fig. 11.** Adjustments of the ISM rainfall trends according to the IPO phase transition. (a) EM of the IPO-adjusted
1018 internal JJA rainfall trends ($\partial_t pr_{internal_adj}$) in ESPPE during 1950-1999, representing the rainfall trend caused by
1019 the observed IPO phase transition. (b) EM of the IPO-adjusted total JJA rainfall trends ($\partial_t pr_{adj}$) in ESPPE during
1020 1950-1999, representing the rainfall trend caused by both the external forcing and the observed IPO. (c) Histograms
1021 (bars) and fitted distribution with 100 bins (lines) of the area-averaged rainfall trends over the NCI region during
1022 1950-1999 derived from the 57 ESPPE members. The blue bars and the fitted blue curves show the frequency of
1023 occurrence of the original rainfall trends, with the blue dot and horizontal blue line denote the EM and STD of $0.01 \pm$
1024 0.14 . The red bars and the fitted red curves show the frequency of occurrence of the rainfall trends with adjustments
1025 accounting for the influence of the observational IPO phase transition (red dot and horizontal red line denote the EM
1026 and STD of -0.15 ± 0.13 . (d-f) are same as (a-c) but for 1999-2013. The EM and STD for the blue and red bars in
1027 (f) are 0.42 ± 0.61 and 0.68 ± 0.54 , respectively. The black dashed lines in (c) and (f) denote the observed NCI
1028 rainfall trends of -0.11 and 0.66, respectively. Units: $\text{mm day}^{-1} \text{decade}^{-1}$.

1029

1030

1031 **Fig. 12.** Spatial patterns of 9-year running-mean JJA rainfall trends during the period of (a) 1950-1999 and (b) 1999-
1032 2013 derived from the EM of the 100-member MPI-ESM ensemble. The STD of the rainfall trends among the 100
1033 MPI-ESM members for (c) 1950-1999 and (d) 1999-2013. Rainfall trends derived from (e) the 10 members with the
1034 strongest positive IPO phase transition (Pos10) during 1950-1999, (f) the 10 members with the strongest negative
1035 IPO phase transition (Neg10) during 1999-2013. Units: $\text{mm day}^{-1} \text{decade}^{-1}$. Slant hatching denotes trends significant
1036 at the 95% confidence level. (g) Time series of the 9-year running-mean of JJA rainfall anomalies averaged over NCI.
1037 Units: mm day^{-1} . Black is for the OBS. Red line and shading denote the EM and 5th and 95th percentile of the 100
1038 members. Brown and blue solid lines represent the mean of Pos10 and Neg10 members during 1950-1999 and 1999-
1039 2013, respectively. Brown and blue dashed lines represent the mean difference of the Pos10 minus EM during 1950-

1040 1999 and the Neg10 minus EM during 1999-2013.

1041

1042

1043 **Fig. 13.** The regression pattern of the internal SST trends with respect to the NCI rainfall trends across 100 members
1044 through the member index: (a) 1950-1999 and (b) 1999-2013 (units: K (decade)⁻¹). Slant hatching denotes regions
1045 significant at the 95% confidence level. (c) EM of the IPO-adjusted internal JJA rainfall trends ($\partial_t pr_{internal_adj}$) in
1046 MPI-ESM during 1950-1999, representing the rainfall trend caused by the observed IPO phase transition. (d) EM of
1047 the IPO-adjusted total JJA rainfall trends ($\partial_t pr_{adj}$) in MPI-ESM during 1950-1999, representing the rainfall trend
1048 caused by both the external forcing and the observed IPO. (e-f) are same as (c-d) but for 1999-2013. Units: mm day
1049 ⁻¹ decade⁻¹.

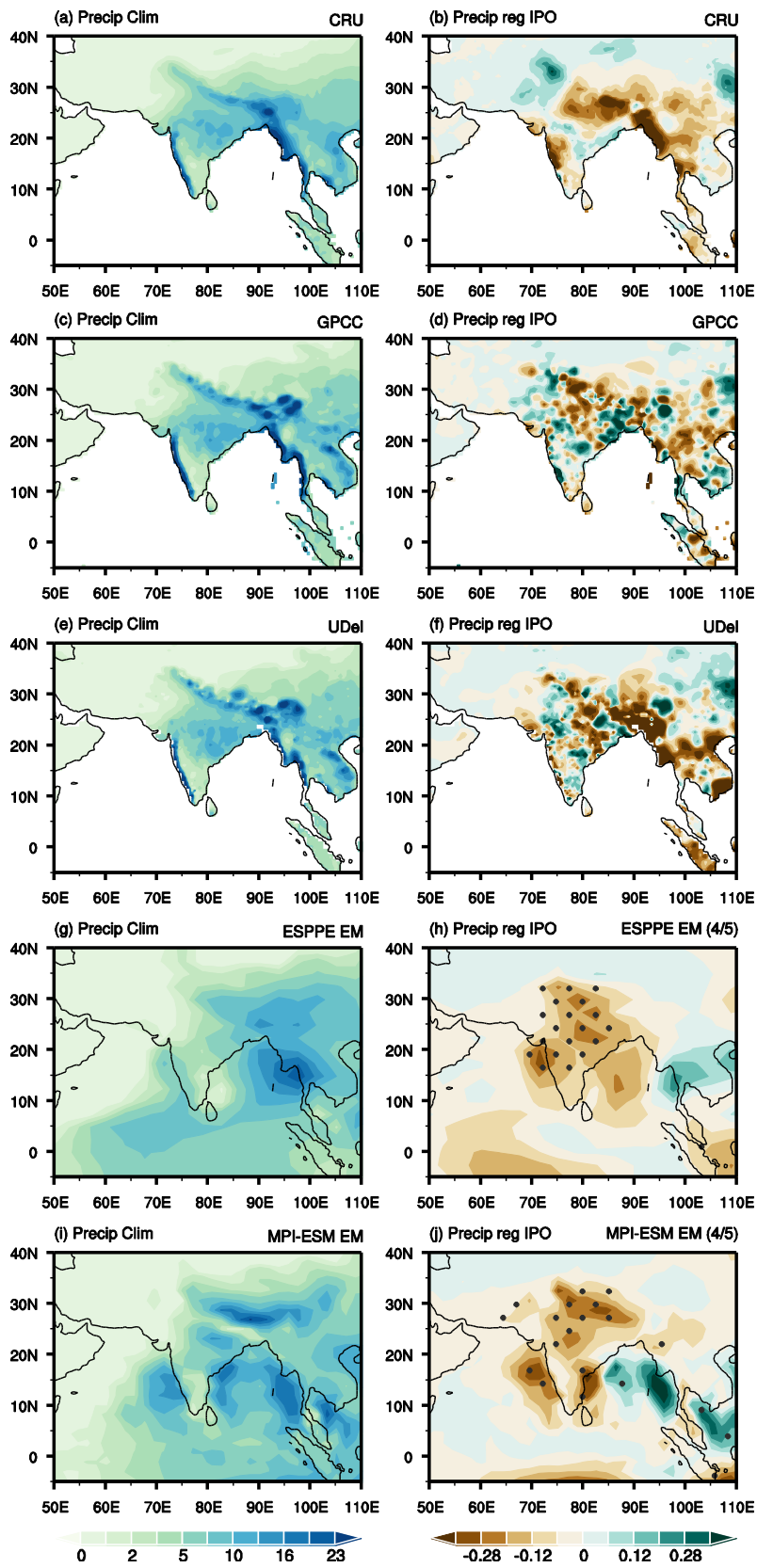
1050

1051

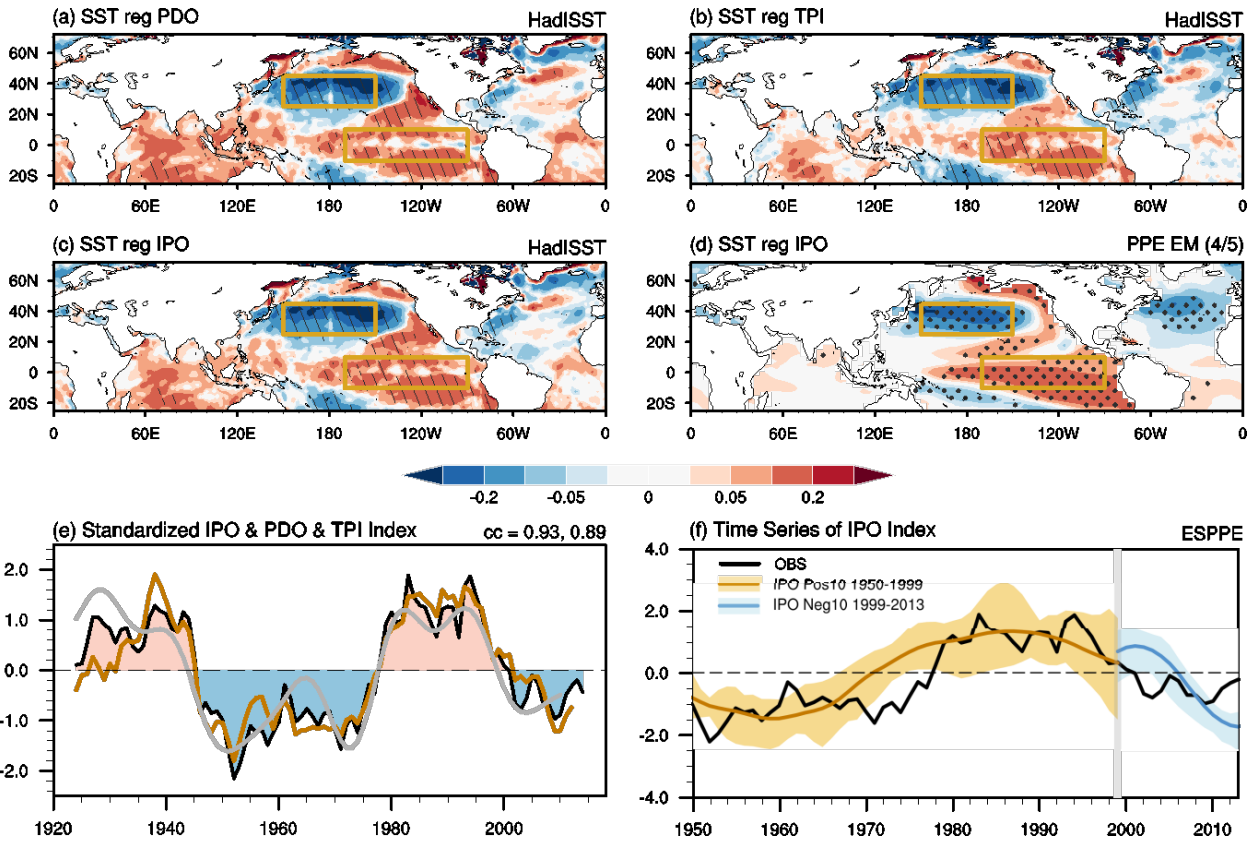
1052 **Fig. 14.** Schematic diagrams showing how external forcing and internal variability affect the recent decline and
1053 recovery of ISM rainfall, respectively.

1054

1055



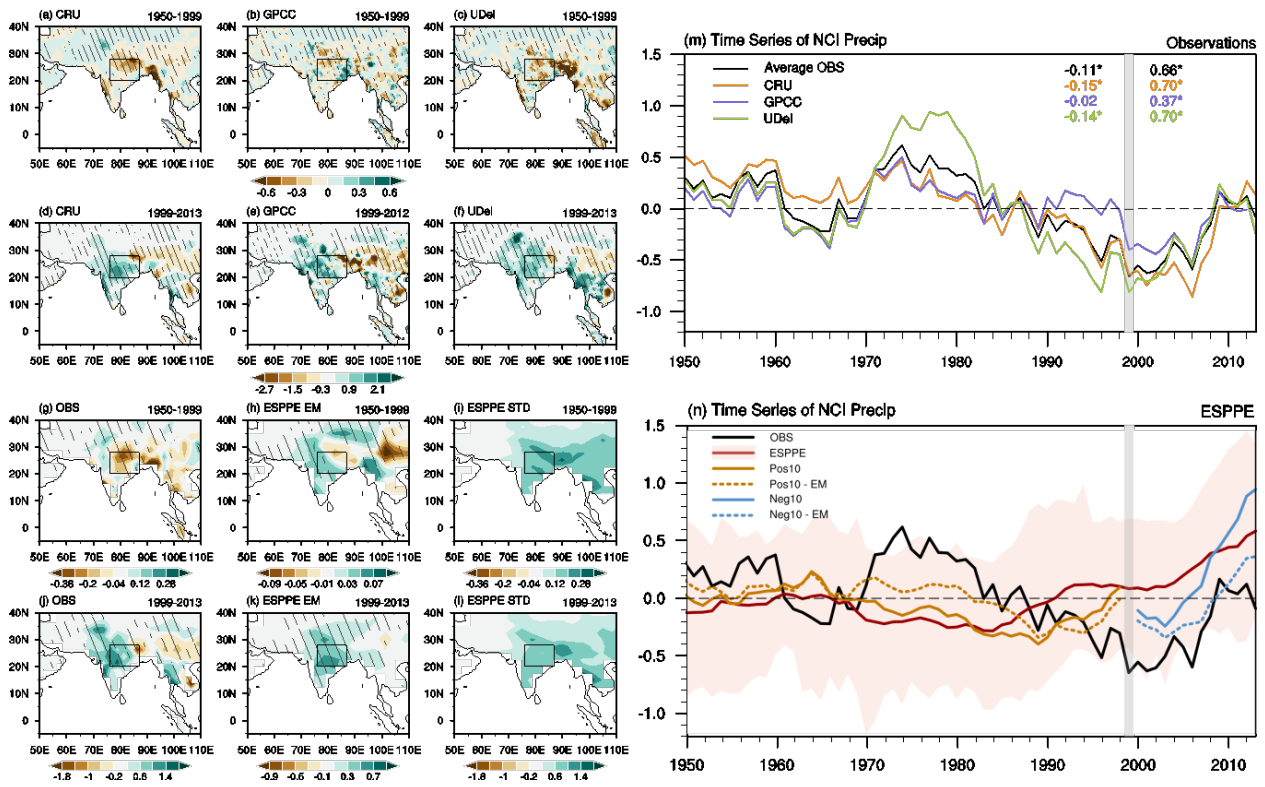
1058 **Fig. 1.** Evaluation of the ESPPE and MPI-ESM in simulating climatological June-July-August (JJA) Indian summer
1059 monsoon (ISM) rainfall and its relation to IPO. (a) CRU, (c) GPCC, (e) UDel, (g) ESPPE ensemble mean and (i)
1060 MPI-ESM ensemble mean (EM) climatological JJA mean rainfall over ISM region in 1950-2013. Regressed 9-year
1061 running mean JJA rainfall with respect to the observed IPO index during 1950-2013: (b) CRU, (d) GPCC and
1062 (f) UDel. (d) ESPPE and (f) MPI-ESM EM of the regressed internal component of JJA 9-year running mean
1063 rainfall onto the IPO index within each ensemble member during 1950-2013. Stippling denotes 4 of 5 ensemble
1064 members agreeing on the sign of change. Units: mm day⁻¹.
1065



1067

1068 **Fig. 2.** Regressed 9-year running-mean JJA SST anomalies from HadISST (units: K) with respect to standardized 9-
 1069 year running-mean (a) PDO index, (b) TPI index and (c) IPO index during the period of 1920-2013. (d) ESPPE EM
 1070 of regressed 9-year running mean JJA SST with respect to standardized IPO index within each member during the
 1071 period of 1920-2013. Slant hatching denotes regional signals significant at the 95% confidence level. Stippling
 1072 denotes 4 of the 5 ensemble members in agreement on the sign of change. (e) Standardized time series of observed
 1073 IPO index (defined as 9-year running-mean SST gradients between TCEP and NP, positive in red and negative in
 1074 blue), standardized 9-year running-mean PDO (orange) and TPI (grey) index. The correlation coefficients between
 1075 the IPO and PDO or TPI indexes are 0.93 and 0.89 ($p < 0.01$), respectively, during the historical period of 1920-
 1076 2013. (f) Time series of IPO index from different ESPPE members. Black, brown and blue lines denote the IPO
 1077 indices derived from HadISST observations and the 10 members with the strongest positive (Pos10) and the strongest
 1078 negative (Neg10) transitions, respectively. The 10 members are chosen separately for both periods of 1950-1999 and
 1079 1999-2013. Light brown and blue shadings show the spread among the 10 members.

1080



1081

1082

1083

1084

1085

1086

1087

1088

1089

1090

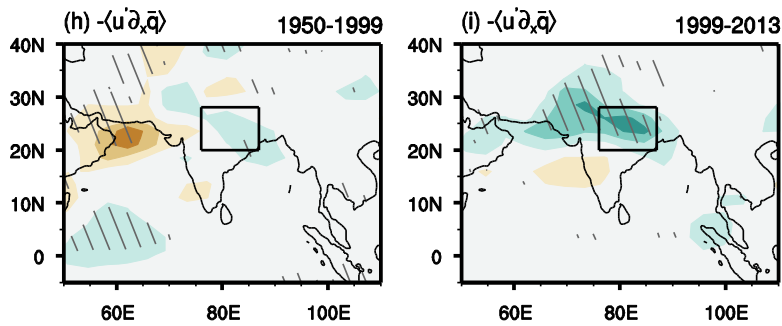
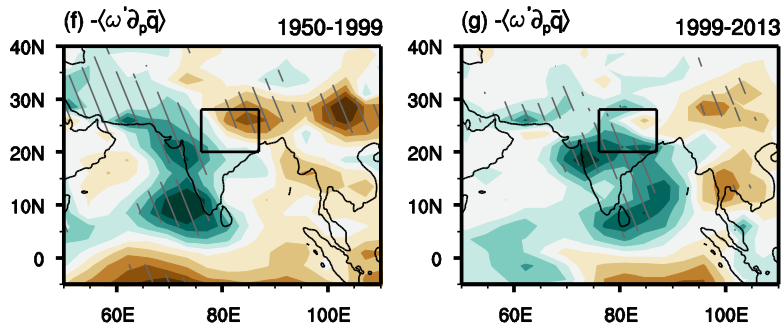
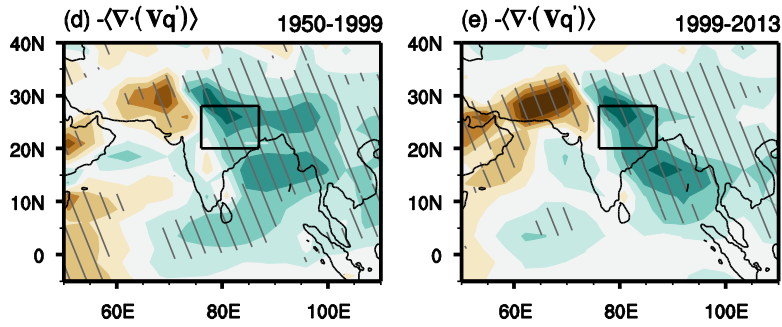
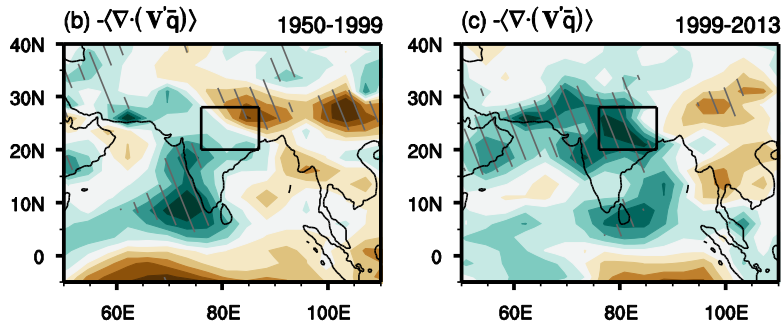
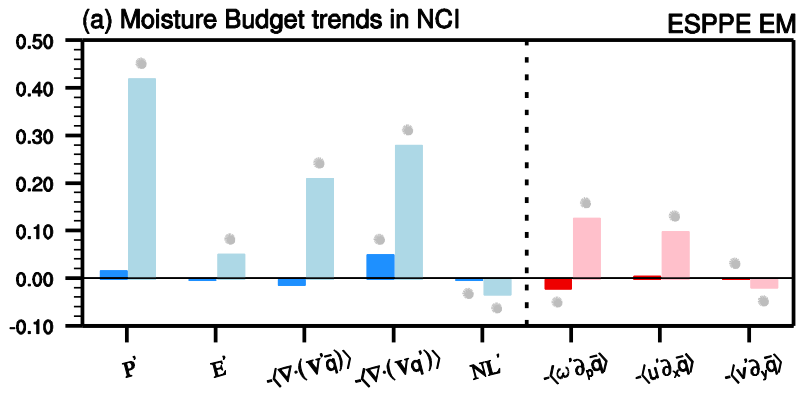
1091

1092

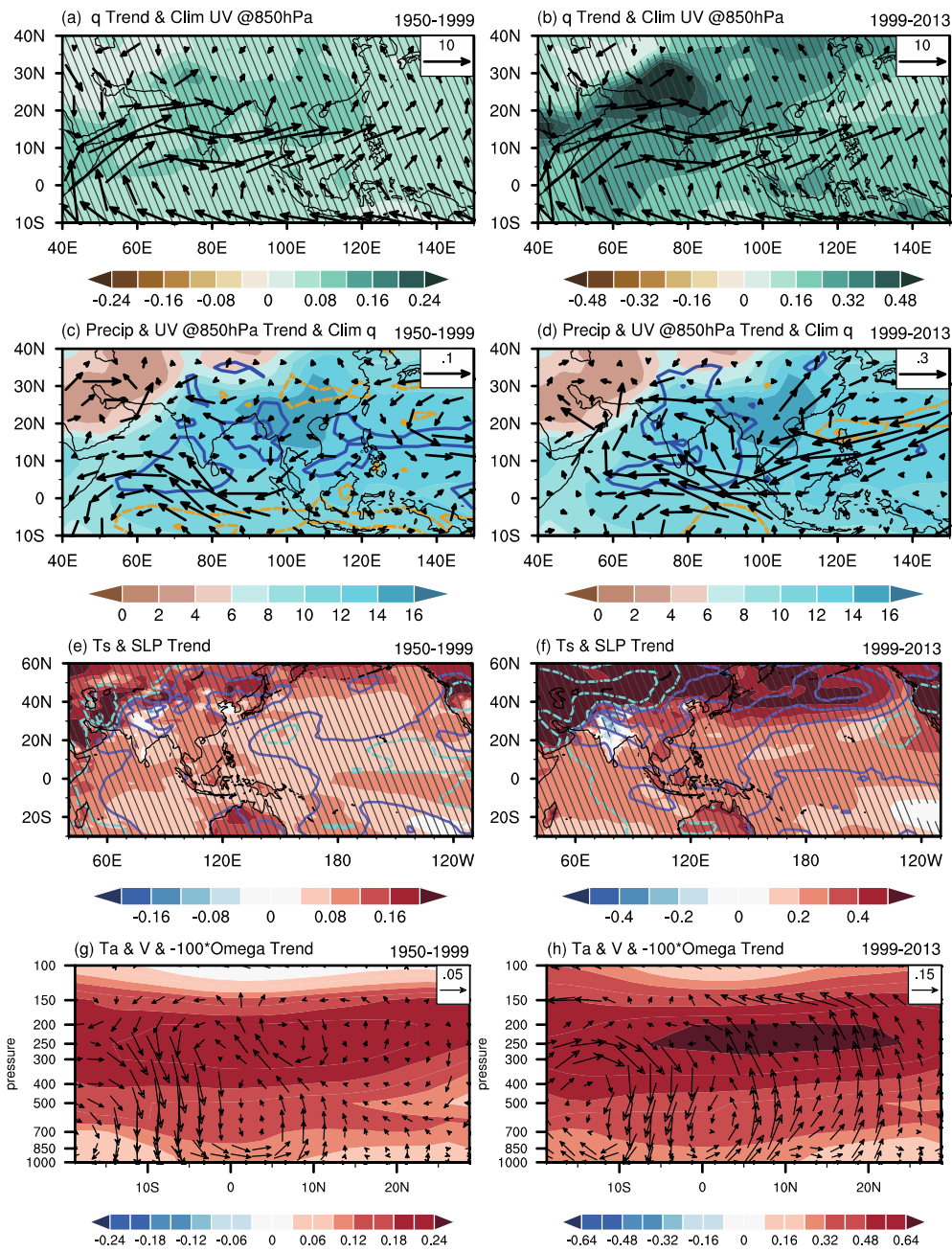
1093

1094

Fig. 3. Spatial patterns of 9-year running-mean JJA rainfall trends during the period of 1950-1999 derived from the (a) CRU, (b) GPCC, (c) UDel, (g) the average OBS and (h) the ESPPE EM. (i) The standard deviation (STD) of the rainfall trends among the 57 ESPPE members for 1950-1999. (d, e, f, j, k, l) are same as (a, b, c, g, h, i) but for 1999-2013. Units: $\text{mm day}^{-1} \text{decade}^{-1}$. Slant hatching denotes rainfall trends significant at the 95% confidence level. (m-n) Time series of the 9-year running-mean JJA rainfall anomalies relative to 1950-2013 mean average over north-central India (NCI; 20°N – 28°N , 76°E – 87°E) outlined by the rectangle in (a-l). Units: mm day^{-1} . In (m), colours of orange, purple, green and black represent the CRU, GPCC, UDel datasets and their average (referred to as OBS), respectively. The coloured numbers in (m) denote the NCI rainfall trends of corresponding datasets during both periods. In (n), black is for the OBS. Red line and shading denote the EM and 5th and 95th percentile of the 57 members. Brown and blue solid lines represent the mean of 10 members with strongest positive (Pos10) and the strongest negative (Neg10) IPO transitions during 1950-1999 and 1999-2013, respectively. Brown and blue dashed lines represent the mean difference of the Pos10 minus EM during 1950-1999 and the Neg10 minus EM during 1999-2013.



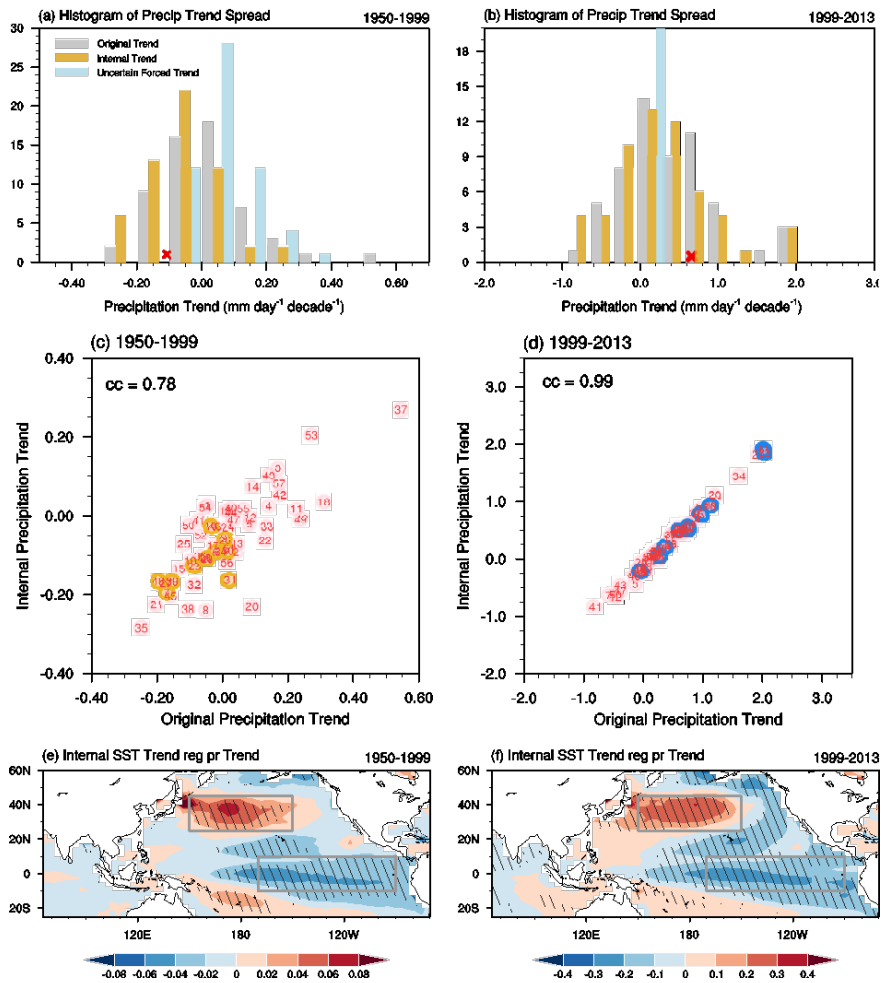
1096 **Fig. 4.** Moisture budget analysis of the external forced rainfall trend derived from the ESPPE EM. (a). Moisture
1097 budget analysis on EM NCI rainfall trend (dots denote trend differences significant at 95% confidence level) during
1098 1950-1999 (dark color bars) and 1999-2013 (light color bars). Rainfall change is balanced by the changes of
1099 evaporation, dynamic and thermodynamic components and a nonlinear term (blue and light blue bars). The dynamic
1100 component is further separated into vertical, zonal and meridional dynamic components of moisture convergence
1101 (red and pink bars). (b, d, f, h) are spatial patterns of EM trend during 1950-1999 of dynamic component,
1102 thermodynamic component, vertical dynamic component and zonal dynamic component of moisture advection,
1103 respectively. (c, e, g, i) are same as (b, d, f, h) but for 1999-2013. Units: $\text{mm day}^{-1} \text{decade}^{-1}$. Slant hatching denotes
1104 regions significant at 95% confidence level.
1105



1106

1107 **Fig. 5.** (a) Trend of EM JJA 850hPa specific humidity (shading, units: $\text{g kg}^{-1} \text{ decade}^{-1}$) and EM climatological 850hPa
 1108 winds (vectors, units: m s^{-1}) from 1950-1999. (c) EM climatological JJA 850hPa specific humidity (shading, units: g
 1109 kg^{-1}) and trend of EM rainfall (contours, positive in solid blue lines and negative in dashed brown lines; units: mm
 1110 $\text{day}^{-1} \text{ decade}^{-1}$) and 850hPa winds (vectors, units: $\text{m s}^{-1} \text{ decade}^{-1}$) from 1950-1999. (e) Trend of EM JJA near surface
 1111 temperature and SST (shading, units: K decade^{-1}) and sea level pressure (contours, positive in solid purple lines and
 1112 negative in dashed cyan lines; units: Pa decade^{-1}). (g) Cross section of zonally-averaged (65°E – 95°E) trend of EM
 1113 air temperature (shading, units: K decade^{-1}) and winds (vectors, meridional and vertical components; units: m s^{-1}
 1114 decade^{-1}). The vertical component is calculated with a scale factor of -100 to allow the vertical pressure-velocity to

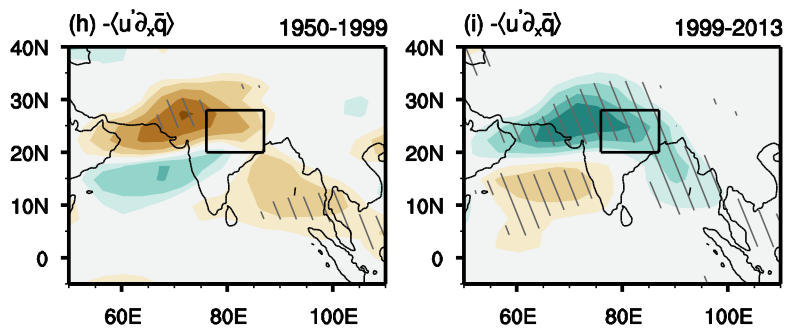
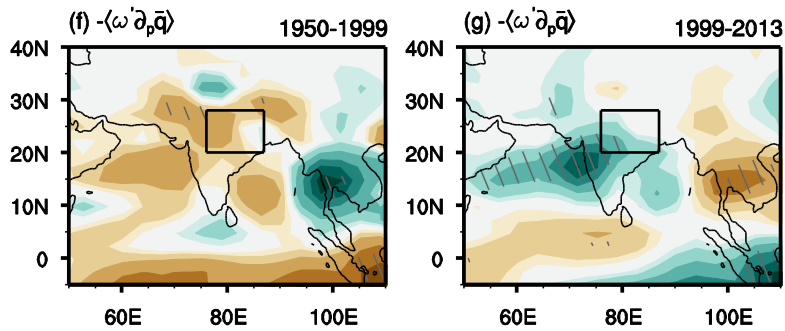
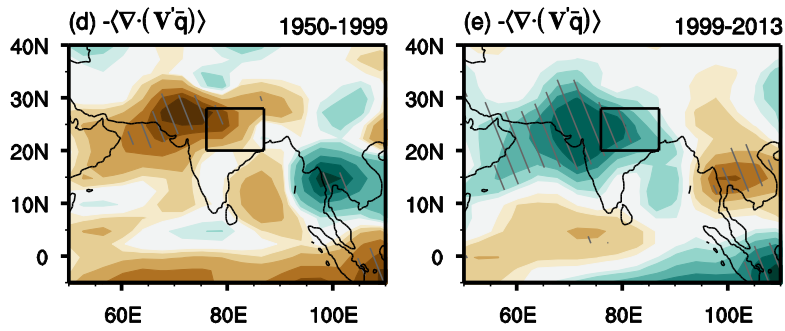
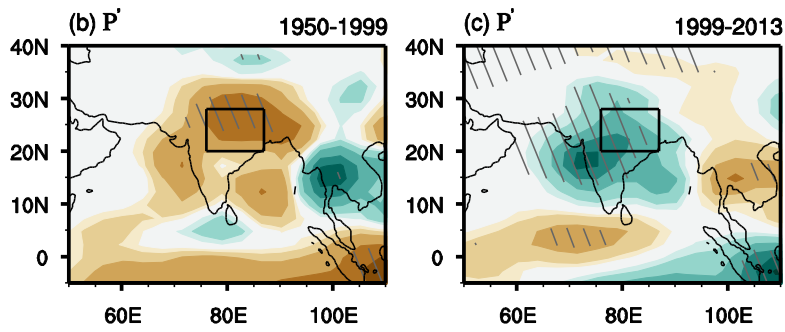
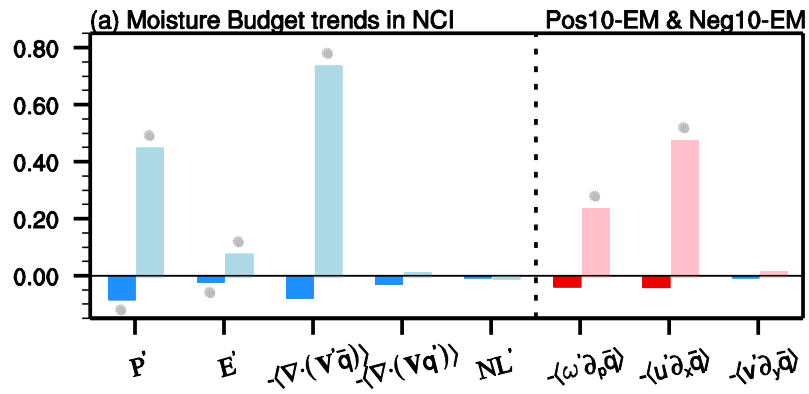
1115 be comparable with the meridional component. (b, d, f, h) are same as (a, c, e, g) but for 1999-2013. Slant hatching
1116 denotes regions significant at 95% confidence level.
1117



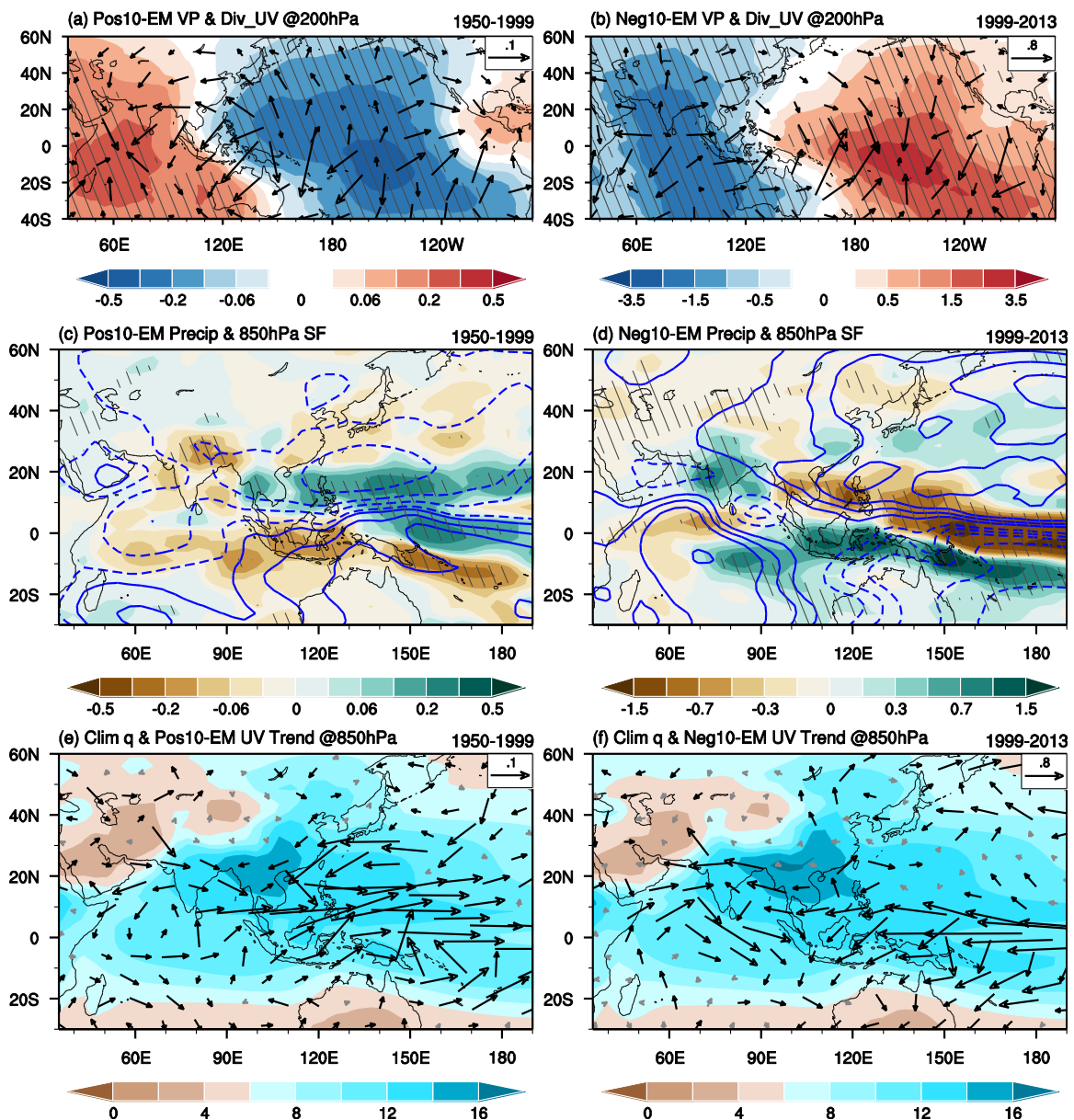
1118

1119 **Fig. 6.** Histograms of spread in NCI rainfall trends among 57 members during (a) 1950-1999 and (b) 1999-2013
 1120 (grey, yellow and blue bars denote the trends of the original rainfall, the internal component and the uncertain-forced
 1121 component of rainfall). Correlation between trends of the original rainfall (x-bar, units: $\text{mm day}^{-1} \text{decade}^{-1}$) and the
 1122 internal component of the rainfall (y-bar, units: $\text{mm day}^{-1} \text{decade}^{-1}$) over the NCI region derived from ESPPE
 1123 members (number indicated in the circle) during the period (c) 1950-1999 and (d) 1999-2013. (The outlined member
 1124 “37” in c. is caused by the combination of a positive internal rainfall trend and an evidently positive forced trend.)
 1125 Brown circles in (c) denote the 10 members with the strongest positive IPO phase transition during 1950-1999. Blue
 1126 circles in (d) denote the 10 members with the strongest negative IPO phase transition during 1999-2013. The
 1127 regression pattern of the internal SST trends with respect to the NCI rainfall trends across 57 members through the
 1128 member index: (e) 1950-1999 and (f) 1999-2013 (units: $\text{K} (\text{decade})^{-1}$). Slant hatching denotes regions significant at
 1129 the 95% confidence level. The rectangles in (e-f) outline the tropical central-eastern Pacific (TCEP, 170°W – 90°W ,
 1130 10°S – 10°N) and the North Pacific (NP, 150°E – 150°W , 25°N – 45°N).

1131



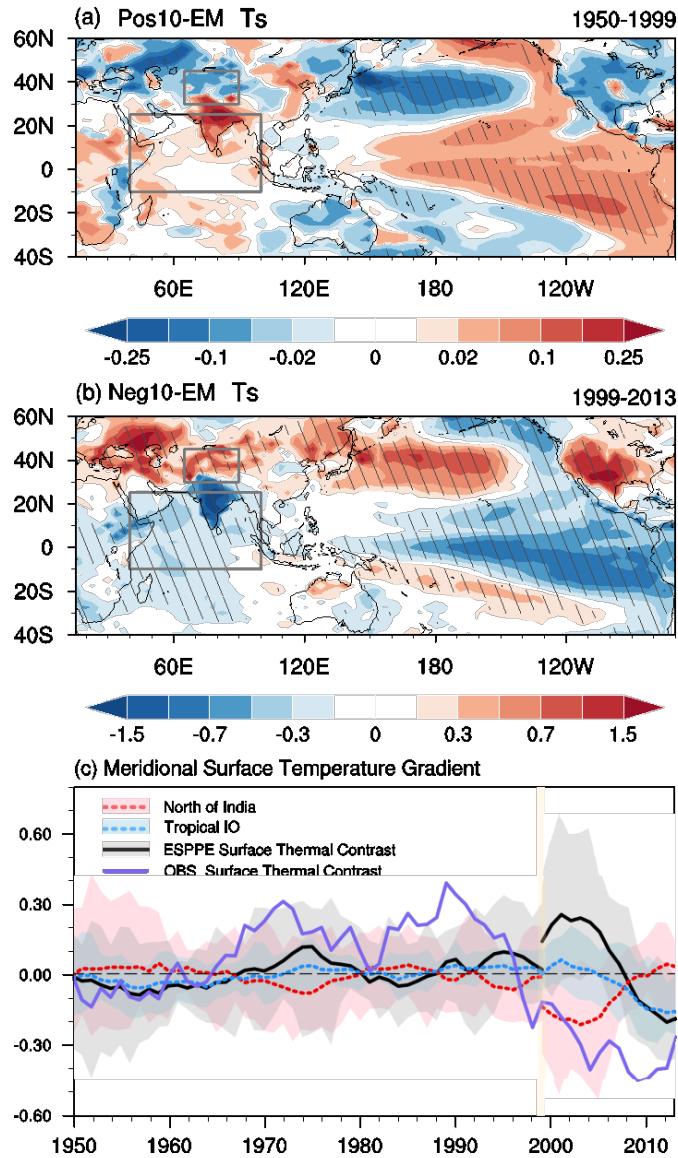
1133 **Fig. 7.** Moisture budget analysis of the rainfall trend related to IPO phase transitions. (a). Moisture budget analysis
1134 on NCI rainfall trend difference between the 10 members with the strongest positive IPO phase transition and
1135 ensemble mean during 1950-1999 (Pos10-EM; dark colour bars). Light colour bars are for Neg10-EM during 1999-
1136 2013. Dots denote trend differences significant at 95% confidence level. Rainfall change is balanced by the changes
1137 of evaporation, dynamic and thermodynamic components and a nonlinear term (blue and light blue bars). The
1138 dynamic component is further separated into vertical, zonal and meridional dynamic components of moisture
1139 advection (red and pink bars). (b, d, f, h) are spatial patterns of Pos10-EM trend during 1950-1999 of rainfall, dynamic
1140 component, vertical dynamic component and zonal dynamic component of moisture advection, respectively. (c, e, g,
1141 i) are same as (b, d, f, h) but for Neg10-EM during 1999-2013. Units: $\text{mm day}^{-1} \text{ decade}^{-1}$. Slant hatching denotes
1142 regions significant at 95% confidence level.
1143



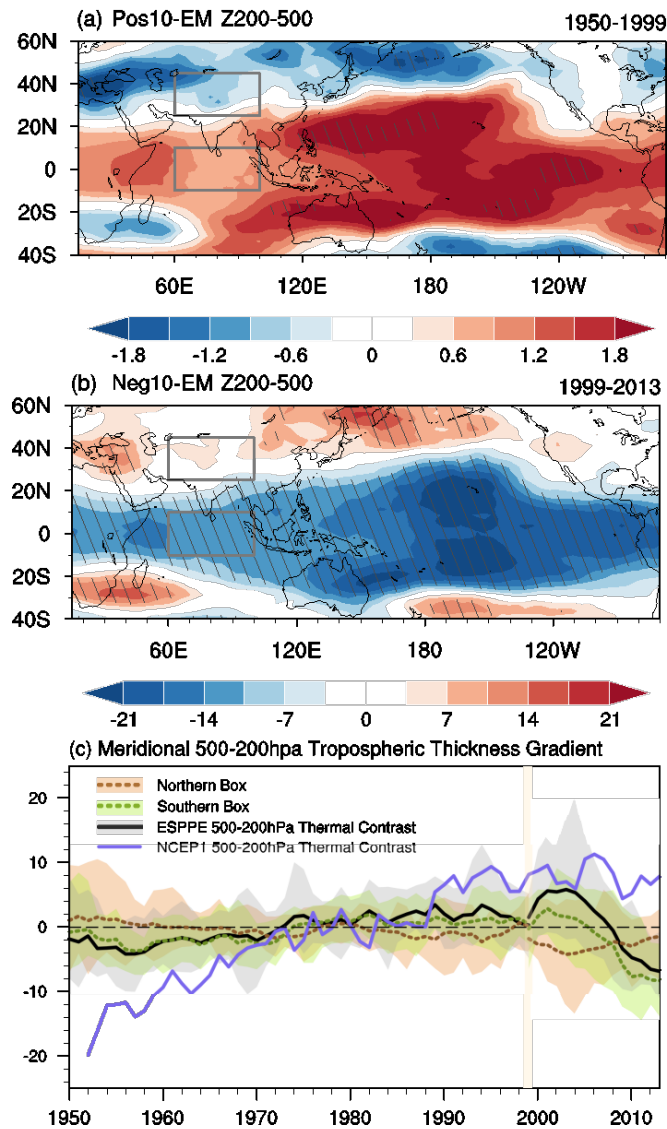
1144

1145 **Fig. 8.** Mechanisms of IPO's modulation of ISM rainfall reduction and revival. JJA trend differences between the 10
 1146 members with the strongest positive IPO phase transition and ensemble mean (Pos10-EM) from 1950-1999 for: (a)
 1147 velocity potential (shading, units: $\text{m}^2 \text{s}^{-1} \text{decade}^{-1}$) and divergent winds (vectors, units: $\text{m s}^{-1} \text{decade}^{-1}$) at 200hPa; (c)
 1148 rainfall (shading, units: $\text{mm day}^{-1} \text{decade}^{-1}$) and 850hPa stream function anomalies (contours, units: $10^6 \text{m}^2 \text{s}^{-1} \text{decade}^{-1}$);
 1149 (e) 850hPa winds (vectors, units: $\text{m s}^{-1} \text{decade}^{-1}$) and climatological specific humidity (shading, units: g/kg). (b),
 1150 (d) and (f) are the same as (a), (c) and (e) but for Neg10-EM trend differences in 1999-2013. Slant hatching denotes
 1151 regions significant at 95% confidence level.

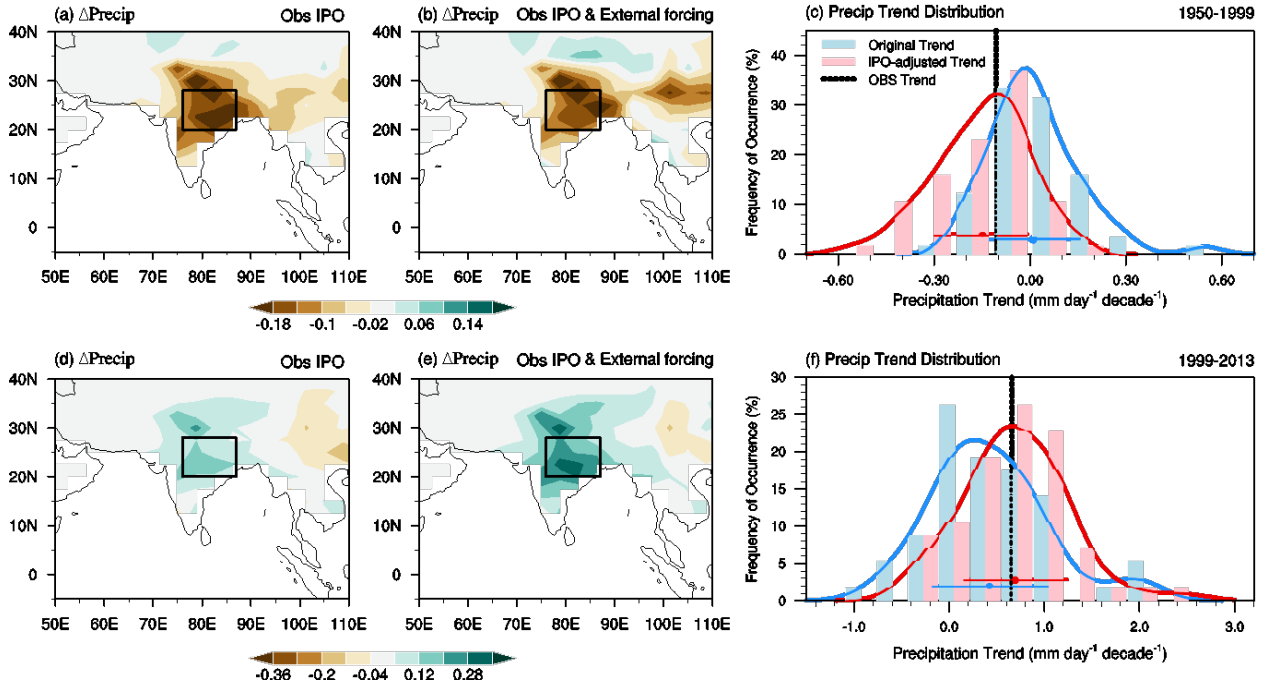
1152



1153
 1154 **Fig. 9.** JJA surface temperature trend related to IPO phase transitions. (a) Spatial patterns of the trend differences of
 1155 the JJA surface temperature between the 10 members with the strongest positive IPO phase transition and ensemble
 1156 mean (Pos10-EM) during 1950-1999. (b) is the same as (a) but for trend differences of Neg10-EM during 1999-2013.
 1157 (c) Composite 9-year running mean anomalies (relative to 1950-2013 mean) derived from the Pos10-EM composite
 1158 difference for 1950-1999 and the Neg10-EM composite difference for 1999-2013 for surface air temperature over
 1159 the landmass north of India (red, land area in 30°N–45°N, 65°E–90°E), SST over the tropical Indian Ocean (blue,
 1160 ocean area over the 10°S–25°N, 40°E–100°E) and the land-sea thermal contrast (black, i.e., the difference between
 1161 the red and blue lines). The purple line denotes the observed land-sea surface thermal contrast derived from the
 1162 CRUTEM4 and HadISST datasets.
 1163



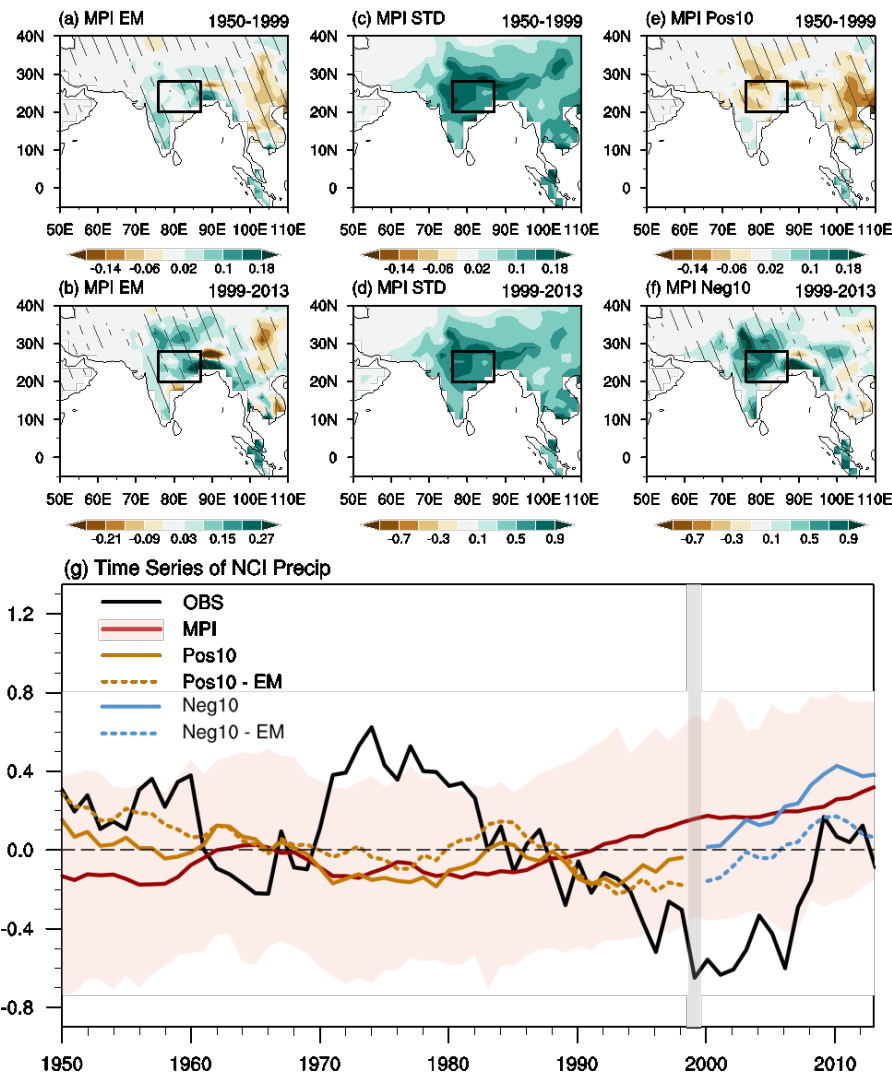
1164
 1165 **Fig. 10.** JJA mid-upper tropospheric thickness trend related to IPO phase transitions. (a) Spatial patterns of the trend
 1166 differences of the JJA 500-200hPa tropospheric thickness between the 10 members with the strongest positive and
 1167 the ensemble mean (Pos10-EM) during 1950-1999. (b) is the same as (a) but for trend differences of Neg10-EM
 1168 during 1999-2013. (c) Composite 9-year running mean anomalies (relative to 1950-2013 mean) derived from the
 1169 Pos10-EM composite difference for 1950-1999 and the Neg10-EM composite difference for 1999-2013 for 500-
 1170 200hPa tropospheric thickness over Eurasia (brown, the northern box over 25°N–45°N, 60°E–100°E in a-b), the
 1171 tropical Indian Ocean (green, the southern box over 10°S–10°N, 60°E–100°E in a-b) and the meridional thermal
 1172 gradient over India (black, i.e., the difference between the brown and green lines). The purple line denotes the
 1173 meridional 500-200hPa tropospheric thickness gradient derived from the NCEP/NCAR reanalysis.
 1174



1175
 1176 **Fig. 11.** Adjustments of the ISM rainfall trends according to the IPO phase transition. (a) EM of the IPO-adjusted
 1177 internal JJA rainfall trends ($\partial_t pr_{internal_adj}$) in ESPPE during 1950-1999, representing the rainfall trend caused by
 1178 the observed IPO phase transition. (b) EM of the IPO-adjusted total JJA rainfall trends ($\partial_t pr_{adj}$) in ESPPE during
 1179 1950-1999, representing the rainfall trend caused by both the external forcing and the observed IPO. (c) Histograms
 1180 (bars) and fitted distribution with 100 bins (lines) of the area-averaged rainfall trends over the NCI region during
 1181 1950-1999 derived from the 57 ESPPE members. The blue bars and the fitted blue curves show the frequency of
 1182 occurrence of the original rainfall trends, with the blue dot and horizontal blue line denote the EM and STD of $0.01 \pm$
 1183 0.14 . The red bars and the fitted red curves show the frequency of occurrence of the rainfall trends with adjustments
 1184 accounting for the influence of the observational IPO phase transition (red dot and horizontal red line denote the EM
 1185 and STD of -0.15 ± 0.13). (d-f) are same as (a-c) but for 1999-2013. The EM and STD for the blue and red bars in
 1186 (f) are 0.42 ± 0.61 and 0.68 ± 0.54 , respectively. The black dashed lines in (c) and (f) denote the observed NCI
 1187 rainfall trends of -0.11 and 0.66 , respectively. Units: $\text{mm day}^{-1} \text{ decade}^{-1}$.

1188

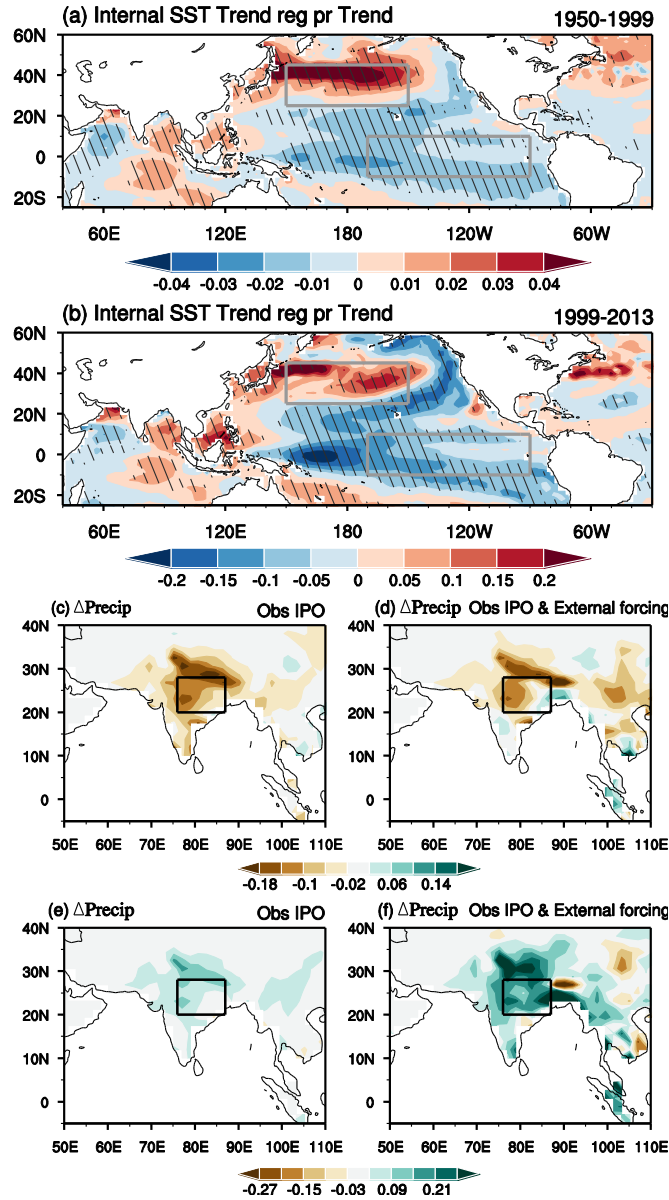
1189



1190
1191

1192 **Fig. 12.** Spatial patterns of 9-year running-mean JJA rainfall trends during the period of (a) 1950-1999 and (b) 1999-
1193 2013 derived from the EM of the 100-member MPI-ESM ensemble. The STD of the rainfall trends among the 100
1194 MPI-ESM members for (c) 1950-1999 and (d) 1999-2013. Rainfall trends derived from (e) the 10 members with the
1195 strongest positive IPO phase transition (Pos10) during 1950-1999, (f) the 10 members with the strongest negative
1196 IPO phase transition (Neg10) during 1999-2013. Units: mm day⁻¹ decade⁻¹. Slant hatching denotes trends significant
1197 at the 95% confidence level. (g) Time series of the 9-year running-mean of JJA rainfall anomalies averaged over NCI.
1198 Units: mm day⁻¹. Black is for the OBS. Red line and shading denote the EM and 5th and 95th percentile of the 100
1199 members. Brown and blue solid lines represent the mean of Pos10 and Neg10 members during 1950-1999 and 1999-
1200 2013, respectively. Brown and blue dashed lines represent the mean difference of the Pos10 minus EM during 1950-
1201 1999 and the Neg10 minus EM during 1999-2013.

1202



1203

1204

1205

1206

1207

1208

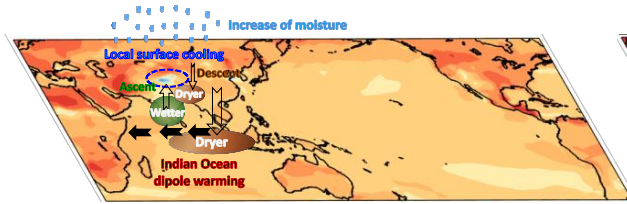
1209

1210

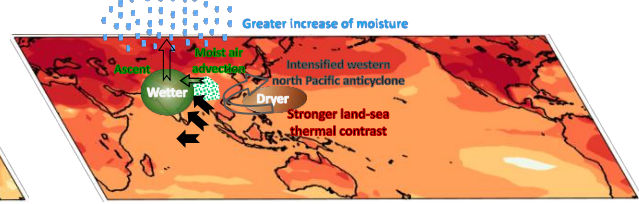
1211

Fig. 13. The regression pattern of the internal SST trends with respect to the NCI rainfall trends across 100 members through the member index: (a) 1950-1999 and (b) 1999-2013 (units: K (decade)⁻¹). Slant hatching denotes regions significant at the 95% confidence level. (c) EM of the IPO-adjusted internal JJA rainfall trends ($\partial_t pr_{internal_adj}$) in MPI-ESM during 1950-1999, representing the rainfall trend caused by the observed IPO phase transition. (d) EM of the IPO-adjusted total JJA rainfall trends ($\partial_t pr_{adj}$) in MPI-ESM during 1950-1999, representing the rainfall trend caused by both the external forcing and the observed IPO. (e-f) are same as (c-d) but for 1999-2013. Units: mm day⁻¹ decade⁻¹.

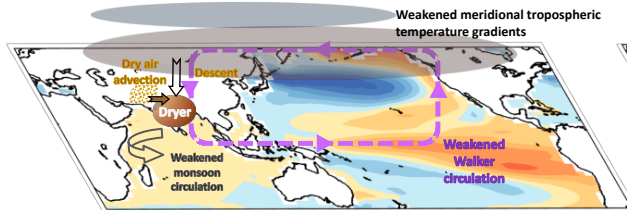
(a) External forcing (1950-1999)



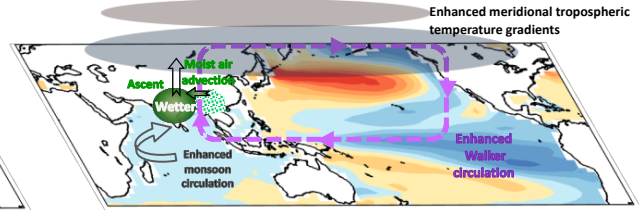
(b) External forcing (1999-2013)



(c) Internal variability (1950-1999)



(d) Internal variability (1999-2013)



1212

1213 **Fig. 14.** Schematic diagrams showing how external forcing and internal variability affect the recent decline and

1214 recovery of ISM rainfall, respectively.

1215